Four decades of Antarctic surface elevation changes from multi-mission satellite altimetry

Ludwig Schröder[1], Martin Horwath[1], Reinhard Dietrich[1], Veit Helm[2], Michiel R. van den Broeke[3], and Stefan R. M. Ligtenberg[3]

[1]Technische Universität Dresden, Institut für Planetare Geodäsie, Dresden, Germany
[2]Alfred Wegener Institute, Helmholtz Centre for Polar and Marine Research, Bremerhaven, Germany
[3]Institute for Marine and Atmospheric Research Utrecht, Utrecht University, Utrecht, The Netherlands

Correspondence: Ludwig Schröder (ludwig.schroeder@tu-dresden.de)

Abstract. We developed a multi-mission satellite altimetry analysis over the Antarctic Ice Sheet which comprises Seasat, Geosat, ERS-1, ERS-2, Envisat, ICESat and CryoSat-2. After a consistent reprocessing and a stepwise calibration of the inter-mission offsets, we obtain monthly grids of multi-mission surface elevation change (SEC) w.r.t the reference epoch 09/2010. A validation with independent SEC from in situ observations as well as a comparison with a firn model proves that the different missions and observation modes have been successfully combined to a seamless multi-mission time series. For coastal East Antarctica, even Seasat and Geosat provide reliable information and, hence, allow to analyze four decades of elevation changes. The spatial and temporal resolution of our result allows to identify when and where significant changes in elevation occurred. These time series add detailed information to the evolution of surface elevation in key regions as Pine Island Glacier, Totten Glacier, Dronning Maud Land or Lake Vostok. After applying a density mask, we calculated time series of mass changes and find that the Antarctic Ice Sheet north of 81.5°S lost a total mass of -2068±377 Gt between 1992 and 2017.

1 Introduction

Satellite altimetry is fundamental for detecting and understanding changes in the Antarctic ice sheet (AIS, Rémy and Parouty, 2009; Shepherd et al., 2018). Since 1992, altimeter missions have revealed dynamic thinning of several outlet glaciers in West Antarctica and have put narrow limits on elevation changes in most parts of East Antarctica. Rates of surface elevation change are not constant in time. Ice flow acceleration has caused dynamic thinning to accelerate (Mouginot et al., 2014; Hogg et al., 2017). Variations in surface mass balance (SMB) and firn compaction rate also cause interannual variations of surface elevation (Horwath et al., 2012; Shepherd et al., 2012; Lenaerts et al., 2013). Consequently, different rates of change have been reported from altimeter missions that cover different time intervals. For example, ERS-1 and ERS-2 data over the interval 1992-2003 revealed negative elevation rates in eastern Dronning Maud Land and Enderby Land (25-60°E) and positive rates in Princess Elizabeth Land (70-100°E) (Wingham et al., 2006b), while Envisat data over the interval 2003-2010 revealed the opposite pattern (Flament and Rémy, 2012). Two large snowfall events in 2009 and 2011 have induced stepwise elevation changes in Dronning Maud Land (Lenaerts et al., 2013; Shepherd et al., 2012).

In consequence, results derived from a single mission, or even more so, mean linear rates reported from a single mission, have limited significance in characterizing the long-term evolution of the ice sheet (Wouters et al., 2013). Data from different altimeter missions need to be linked over a time span as long as possible in order to better distinguish and understand the long-term evolution and the natural variability of ice sheet volume and mass.

Missions with similar sensor characteristics were combined e.g. by Wingham et al. (2006b, ERS-1 and ERS-2) and Li and Davis (2008, ERS-2 and Envisat). Fricker and Padman (2012) use Seasat, ERS-1, ERS-2 and Envisat to determine elevation changes of Antarctic ice shelves. They apply constant biases, determined over open ocean, to cross-calibrate the missions. In contrast to ocean-based calibration, Zwally et al. (2005) found significant differences for the biases over ice sheets with a distinct spatial pattern (see also Frappart et al., 2016). Also Khvorostovsky (2012) showed that the correction of inter-mission offsets over an ice sheet is not trivial. Therefore, Paolo et al. (2016) cross-calibrated ERS-1, ERS-2 and Envisat on each grid cell, using overlapping epochs, which is very similar to our approach for these missions. Linking different missions becomes even more challenging when different sensor characteristics are concerned, such as ICESat laser altimetry or CryoSat-2 interferometric Synthetic Aperture Radar (SARIn) mode, or when the missions do not overlap in time.

Here we present an approach to combine seven different satellite altimetry missions over the AIS. By a refined waveform retracking and slope correction of the radar altimetry (RA) data we ensure consistency of the surface elevation measurements and improve their precision by up to 50%. In the following stepwise procedure, we first process the measurements from all missions jointly using the repeat altimetry method. We then form monthly time series for each individual mission data set. Finally, we merge all time series. For this last step, we employ different approaches of inter-mission offset estimation, depending on the temporal overlap or non-overlap of the missions and on the similarity or dissimilarity of their altimeter sensors.

We arrive at consistent and seamless time series of gridded surface elevation differences with respect to a reference epoch (09/2010). They represent three-month temporal averages sampled every month and an effective spatial resolution of about 20 km sampled to a 10 km grid. We evaluate our results and their estimated uncertainties by a comparison with independent in situ data sets, results from satellite gravimetry and results from regional atmospheric climate modeling. We illustrate that these time series of surface elevation change (SEC) allow to study geometry changes and derived mass changes of the AIS in unprecedented detail. For some examples as Pine Island Glacier, Totten Glacier, Shirase Glacier (Dronning Maud Land) and Lake Vostok, we demonstrate the benefits of the long time series. Finally, we calculate ice sheet mass balances from these data for the respectively covered regions. A comparison with independent data indicates a high consistency of the different data sets but reveals also remaining discrepancies.

While this paper gives some examples for new insights obtained from the presented multi-mission altimetry analysis, it can not fully exploit all potential applications. This will be the scope of future work with this data set.

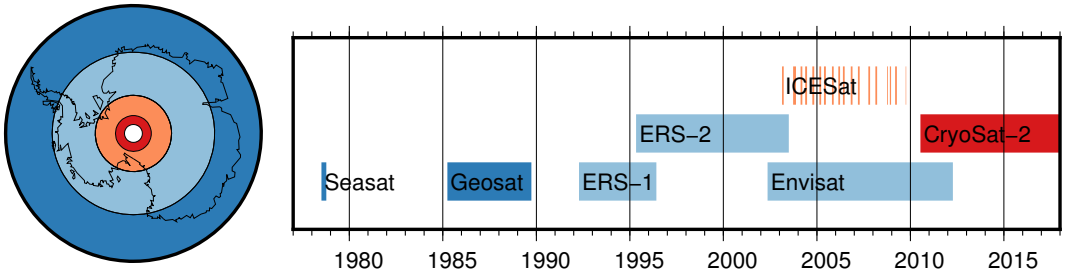

Figure 1. Spatial and temporal coverage of the satellite altimetry data used in this study. The colors denote the maximum southern extent of the measurements (dark blue: 72°S, light blue: 81.5°S, orange: 86°S, red: 88°S) and thus the size of the respective polar gap.

2 Data

2.1 Altimetry data used

We use the ice sheet surface elevation observations from seven satellite altimetry missions: Seasat, Geosat, ERS-1, ERS-2, Envisat, ICESat and CryoSat-2. Figure 1 gives an overview over their temporal and spatial coverage. The data of the two early missions, Seasat and Geosat, were obtained from the Radar Ice Altimetry project at Goddard Space Flight Center (GSFC). For ERS-1, ERS-2, Envisat and CryoSat-2 the most recent ESA products were used. For ICESat the final release from the National Snow and Ice Data Center (NSIDC) was used. Further details concerning the dataset versions used are given in the supplement. The data editing criteria, applied to remove corrupted measurements in a preprocessing step are explained there as well.

As illustrated in Fig. 1, due to the inclination of 108°, Seasat and Geosat measurements cover only the coastal regions of the East Antarctic Ice Sheet (EAIS) and the northern tip of the Antarctic Peninsula Ice Sheet (APIS) north of 72°S, which is about 25% of the total ice sheet area. With the launch of ERS-1, the polar gap was reduced to 81.5°S, resulting in a coverage of 79% of the area. The polar gap is even smaller for ICESat (86°S) and CryoSat-2 (88°S), leading to a nearly complete coverage of the AIS in recent epochs.

ERS-1 and ERS-2 measurements were performed in two different modes, distinguished by the width of the tracking time window and the corresponding temporal resolution of the recorded waveform. The ice mode is coarser than the ocean mode, in order to increase the chance of capturing the radar return from rough topographic surfaces (Scott et al., 1994). While the ice mode was employed for the majority of measurements, a significant number of observations has been performed in ocean mode over Antarctica as well (22% for ERS-1, 2% for ERS-2). We use the data from both modes, as the ocean mode provides a higher precision while the ice mode is more reliable in steep terrain (see Fig. S1 and S3). However, as there is a regionally varying bias between the modes, we treat them as two separate data sets, similar to Paolo et al. (2016).

2.2 Reprocessing of radar altimetry

Compared to measurements over the global oceans, pulse limited radar altimetry (PLRA) over ice sheets requires a specific processing to account for the effects of topography and the dielectric properties of the surface (Bamber, 1994). To ensure

consistency in the analysis of PLRA measurements, processed and provided by different institutions, we applied our own method for retracking and slope correction.

The slope correction is applied to account for the effect of topography within the beam limited footprint (Brenner et al., 1983). Different approaches exist to apply a correction (Bamber, 1994) but it is still a main source of error in RA. In Schröder et al. (2017) we showed the clear superiority of the "relocation method", which tries to relate the measurements to the true measurement position, over the "direct method", which determines a correction for the nadir direction. Roemer et al. (2007) developed a refined relocation method which locates the Point of Closest Approach (POCA) within the approximately 20 km beam limited footprint in a digital elevation model (DEM). We applied this method in our reprocessing chain using the DEM of Helm et al. (2014). The CryoSat-2 measurements, used for this DEM, have a very dense coverage, and hence, very little interpolation is necessary. Compared to the DEM of Bamber et al. (2009), this significantly improves the spatial consistency. We optimized the approach of Roemer et al. (2007) with respect to computational efficiency for the application over the entire ice sheet. Instead of searching the POCA with the help of a moving window of 2 km (which represents the pulse limited footprint) we applied a Gaussian filter with σ=1 km to the DEM to resemble the coverage of a pulse limited footprint. Hence, instead of the closest window average, we can simply search for the closest cell in the smoothed grid, which we use as coarse POCA location. In order to achieve a sub-grid POCA location, we fit a biquadratic function to the satellite-to-surface distance within a 3x3 grid cell environment around the coarse POCA grid cell and determine the POCA according to this function.

The retracking of the return signal waveform is another important component in the processing of RA data over ice sheets (Bamber, 1994). Functional fit approaches (e.g. Martin et al., 1983; Davis, 1992; Legrésy et al., 2005; Wingham et al., 2006b) are well established and allow the interpretation of the obtained waveform shape parameters with respect to surface and sub-surface characteristics (e.g. Lacroix et al., 2008; Nilsson et al., 2015). However, the alternative approach of threshold retrackers has proven to be more precise in terms of repeatability (Davis, 1997; Nilsson et al., 2016; Schröder et al., 2017). A very robust variant is called ICE-1, using the "Offset Center of Gravity" (OCOG) amplitude (Wingham et al., 1986). Compared to the waveform maximum, the OCOG-amplitude is significantly less affected by noise (Bamber, 1994). Davis (1997) compared different retrackers and showed that a threshold based retracker, especially with a low threshold as 10%, produces a remarkably higher precision, compared to functional fit based results. We implemented three threshold levels (10%, 20% and 50%) for the OCOG-amplitude which allowed us to analyze the influence of the choice of this level, similar to Davis (1997).

In addition to PLRA, we also use the SARIn mode data of CryoSat-2, reprocessed by Helm et al. (2014). The difference with respect to the processing by ESA mainly consisted in a refined determination of the interferometric phase and in the application of a threshold retracker (TFMRA).

2.3 Accuracy and precision

The accuracy of RA-derived ice surface elevation measurements has been assessed previously by a crossover comparison with independent validation data such as the ICESat laser observations (Brenner et al., 2007), airborne lidar (Nilsson et al., 2016) or ground based GNSS profiles (Schröder et al., 2017). These assessments revealed that with increasingly rough surface topography, the RA measurements show systematically higher elevations than the validation data. This can be explained by

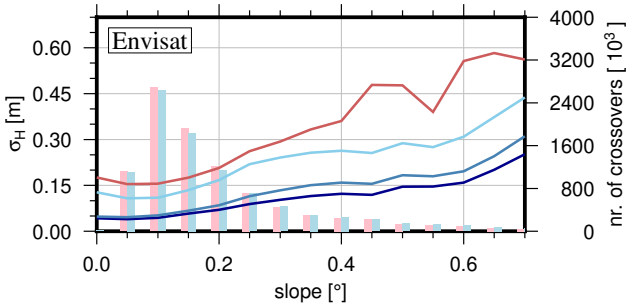

Figure 2. Precision of different processing versions of Envisat measurements from near time (<31 days) crossovers, binned against slope. Red curve: ESA version with ICE-2 retracker and relocated by mean surface slope. Light, medium and dark blue curves: Data reprocessed in this study with 50%-, 20%- and 10%-threshold retracker, respectively, relocated using the refined method. Vertical bars: number of crossovers for the ESA (red) and our 10% threshold retracked data (blue).

the fact that for surfaces that undulate within the ~20 km beam-limited footprint, the radar measurements tend to refer to local topographic maxima (the POCA), while the validation data from ground-based GNSS profiles or ICESat-based profiles represent the full topography. Besides these systematic offsets, also the standard deviation of differences between RA data and validation data is influenced by the surface roughness due to the significantly different sampling of the topography. While over flat terrains, most altimeter satellites perform better than 50 cm, in coastal regions the standard deviations can reach ten meters and more. However, both types of error relate to the different sampling of topography of the respective observation techniques. An elevation change, detected from within the same technique, is not influenced by these effects. Hence, with respect to elevation changes, not the accuracy but the precision (i.e. the repeatability) has to be considered.

This precision can be studied using intra-mission crossovers between ascending and descending profiles. Here, the precision of a single measurement is obtained by $\sigma_H = |\Delta H|/\sqrt{2}$ as two profiles contribute to this difference. To reduce the influence of significant real surface elevation changes between the two passes, we consider only crossovers with a time difference of less than 31 days. In stronger inclined topography, the precision of the slope correction dominates the measurement error (Bamber, 1994). Hence, to provide meaningful results, the surface slope needs to be taken into consideration. We calculate the slope from the CryoSat-2 DEM (Helm et al., 2014). The absence of slope-related effects on flat terrain allows to study the influence of the retracker (denoted as noise here). With increasing slope, the additional error due to topographic effects can be identified.

A comparison of the crossover errors of our reprocessed data and of the respective standard products (see supplement for details) shows significant improvements achieved by our reprocessing. Figure 2 shows this comparison for Envisat (similar plots for each data set can be found in the supplement Fig. S1), binned into groups of 0.05° of specific surface slope. The results for a flat topography show that a 10% threshold provides the highest precision, confirming the findings of Davis (1997). For higher slopes, we see that also our refined slope correction contributed to a major improvement. A constant noise level σ_{noise} and a quadratic, slope related term σ_{slope} has been fitted to the respective data according to $\sigma_H = \sigma_{noise} + \sigma_{slope} \cdot s^2$, where s is in the unit of degrees. The results in Tab. 1 show that for each of the PLRA data sets of ERS-1, ERS-2 and Envisat,

Table 1. Noise level and slope related component (s in degrees) of the measurement precision, fitted to near time crossovers (unit: m) of the data from the respective data center and our reprocessed data (with a 10% threshold retracker applied).

Data set	Data center	Reprocessed
Seasat	$0.21 + 1.91s^2$	$0.25 + 0.70s^2$
Geosat	$0.17 + 0.86s^2$	$0.18 + 1.16s^2$
ERS-1 (ocean)	$0.25 + 0.90s^2$	$0.09 + 0.18s^2$
ERS-1 (ice)	$0.36 + 2.37s^2$	$0.17 + 0.57s^2$
ERS-2 (ocean)	$0.23 + 0.75s^2$	$0.07 + 0.14s^2$
ERS-2 (ice)	$0.38 + 2.57s^2$	$0.15 + 0.53s^2$
Envisat	$0.17 + 1.03s^2$	$0.05 + 0.37s^2$
ICESat	$0.05 + 0.25s^2$	
CryoSat-2 (LRM)	$0.18 + 2.46s^2$	$0.03 + 1.06s^2$
CryoSat-2 (SARIn)	$0.38 + 2.01s^2$	$0.11 + 0.79s^2$

Note that the slope dependent component is weakly determined for data sets with a poor tracking in rugged terrain such as Seasat, Geosat or the ERS ocean mode and for the LRM mode of CryoSat-2.

the measurement noise could be reduced by more than 50% compared to the ESA product (using the functional fit retracker ICE-2, see Legrésy and Rémy, 1997). With respect to the CryoSat-2 CFI retracker (Wingham et al., 2006a), the improvement is even larger. Improvements are also significant for the slope-related component. For the example of Envisat and a slope of 1°, the slope-related component is 1.03 m for the ESA product and only 0.37 m for the reprocessed data. The advanced interferometric processing of the SARIn data achieved similar improvements. For the two early missions Seasat and Geosat, the crossover error of our reprocessed profiles is similar to that of the original dataset from GSFC. However, the number of crossover points is significantly increased, especially for Geosat (see Fig. S1). This means that our reprocessing obtained reliable data where the GSFC processor already rejected the measurements.

In addition to measurement noise, reflected in the crossover differences, a consistent pattern of offsets between ascending and descending tracks has been observed previously (A-D bias, Legrésy et al., 1999; Arthern et al., 2001). Legrésy et al. (1999) interpret this pattern as an effect of the interaction of the linearly polarized radar signal with wind-induced surface structures, while Arthern et al. (2001) attribute the differences to anisotropy within the snowpack. Helm et al. (2014) showed that a low threshold retracker significantly reduces the A-D bias. We observe a similar major reduction (from ±1 m in some regions for a functional fit retracker to ±15 cm when using a 10% threshold, see Fig. S2). The remaining bias is not larger, in its order of magnitude, than the respective noise. Moreover, near the ice sheet margins, the determination of meaningful A-D biases is complicated by the broad statistical distribution of A-D differences and the difficulty to discriminate outliers. We therefore do not apply a systematic A-D bias as a correction but rather include its effect in the uncertainty estimate of our final result.

3 Multi-mission SEC time series

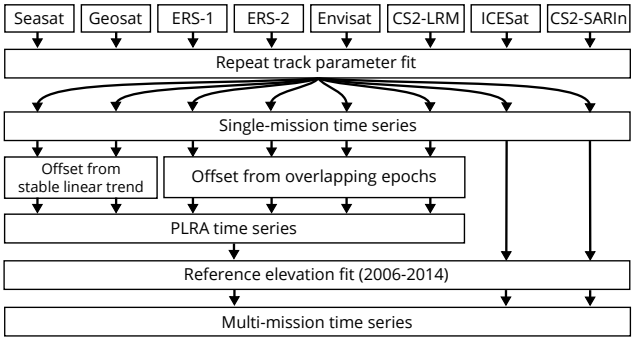

Figure 3. Schematic diagram of the processing steps from the combined repeat track parameter fit over single-mission time series towards a combined multi-mission time series.

3.1 Repeat track parameter fit

We obtain elevation time series following the repeat track approach, similar to Legrésy et al. (2006) and Flament and Rémy (2012). As the orbits of the missions used here have different repeat track patterns, instead of along-track boxes we perform our fit on a regular grid with $1\,\mathrm{km}$ spacing (as in Helm et al., 2014). For each grid cell we analyze all elevation measurements h_i within a radius of $1\,\mathrm{km}$ around the grid cell center. This size seems reasonable as for a usual along track spacing of about $350\,\mathrm{m}$ for PLRA (Rémy and Parouty, 2009), each track will have up to 5 measurements within the radius. Due to the size of the pulse limited footprint a smaller search radius would contain only PLRA measurements with very redundant topographic information and thus would not be suitable to fit a reliable correction for the topography. As specified in Eq. (1), the parameters contain a linear trend (dh/dt), a planar topography (a_0, a_1, a_2) and a regression coefficient (dBS) for the anomaly of backscattered power ($bs_i - \overline{bs}$) to account for variations in the penetration depth of the radar signal.

For a single mission, the parameters are adjusted according to the model

$$\begin{aligned} h_i = \quad & dh/dt(t_i - t_0) + \\ & a_0 + a_1 x_i + a_2 y_i + \\ & dBS(bs_i - \overline{bs}) + \\ & res_i \end{aligned} \tag{1}$$

Here, t_i denotes the time of the observation. The reference epoch t_0 is set to 09/2010. x_i and y_i are the Polar Stereographic coordinates of the measurement location, reduced by the coordinates of the cell's center. The residual res_i describes the misfit between the observation and the estimated parameters.

In contrast to this single mission approach, here we perform a combined processing of all data from different missions and even different altimeter techniques. Thus, some of the parameters may vary between the data sets. To allow for offsets between

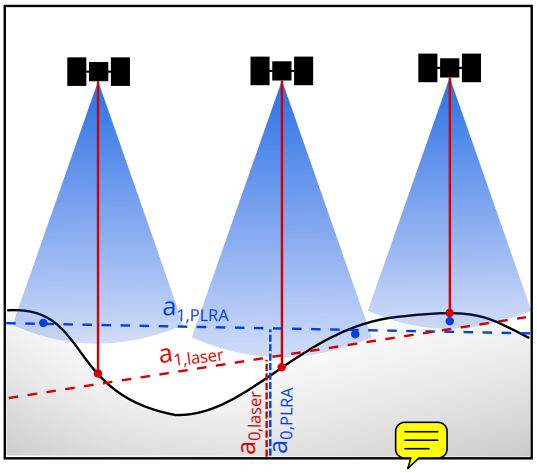

Figure 4. Illustration of the technique-dependent topographic sampling. The laser (red) measures the surface elevation in the nadir of the instrument while for radar altimetry (blue), the first return signal originates from the POCA (marked by the blue point). Hence, planar surface approximations to the measured heights (dashed lines) are intrinsically different for the different techniques.

the missions, the elevation at the cell center a_0 is fitted for each mission individually. The same applies to dBS, which might relate to specific characteristics of a mission as well. For Seasat, covering less than 100 days, this parameter is not estimated, as we assume that during the mission life time no significant changes occurred. For ICESat, dBS is not estimated either, as signal penetration is negligible for the laser measurements.

Between different observation techniques (i.e. PLRA, SARIn and laser altimetry), also the effective surface slope may differ. Considering the specific footprint sizes and shapes, the topography is sampled in a completely different way as illustrated in Fig. 4. While PLRA refers to the closest location anywhere within the ~20 km beam-limited footprint (i.e. the POCA), CryoSat's SARIn measurement can be attributed within the narrow Doppler stripe in cross-track direction. For ICESat the ~70 m laser spot allows a much better sampling of local depressions. Hence, the slope parameters a_1 and a_2 are estimated for each of the techniques independently.

Considering these sensor-specific differences, the model for the least squares adjustment in Eq. (1) is extended for multi-mission processing

$$\begin{aligned} h_i = \quad & dh/dt(t_i - t_0) + \\ & a_{0,M(i)} + a_{1,T(i)} x_i + a_{2,T(i)} y_i + \\ & dBS_{M(i)} (bs_i - \overline{bs_{M(i)}}) + \\ & res_i \end{aligned} \tag{2}$$

where $M(i)$ and $T(i)$ denote to which mission or technique, respectively, the measurement h_i belongs.

We define a priori weights for the measurements h_i based on the precision of the respective mission and mode from crossover analysis (Tab. 1) and depending on the surface slope at the measurement location. This means that in regions with a more distinctive topography, ICESat measurements (with a comparatively low slope-dependent error component) will obtain stronger

weights, compared to PLRA as Envisat. In contrast, over flat regions as on the East Antarctic plateau, the weights are very similar.

3.2 Single-mission time series

After fitting all parameters according to the multi-mission model (Eq. 2), we regain elevation time series by recombining the parameters a_0 and dh/dh with monthly averages of the residuals ($\overline{res}$). For each month j and each mission M, the time series is constructed as

$$h_{j,M} = a_{0,M} + dh/dt(t_j - t_0) + \overline{res_{j,M}}. \tag{3}$$

The elevations $h_{j,M}$ all relate to the cells center and are corrected for time-variable penetration, as the parameters of the topography slope and backscatter correction are omitted in this recombination. Due to the reference elevation $a_{0,M}$, which also contains the inter-mission offsets, this results in individual time series for each single mission. A schematic illustration of the results of this step is given in Fig. 5a. The temporal resolution of these time series is defined by using monthly averages. These $\overline{res}$ represent the anomalies of typically a single satellite pass towards all respective parameters including the linear rate of elevation change. The standard deviation of the residuals in these monthly averages are used as uncertainty measure for $h_{j,M}$ (see C.2 for further details).

3.3 Combination of the single-mission time series

In order to merge data from different missions into a joint time series, inter-mission offsets have to be determined and eliminated. In the ERS reprocessing project (Brockley et al., 2017), mean offsets between the ERS missions and Envisat have been determined and applied to the elevation data. However, for ice sheet studies inter-satellite offsets are found to be regionally varying (Zwally et al., 2005; Thomas et al., 2008; Khvorostovsky, 2012). When merging data from different observation techniques (PLRA, SARIn and laser) the calibration gets even more challenging. We chose an approach in different steps which is depicted in Figs. 3 and 5. Further details concerning the processing of each step can be found in the supplement.

3.3.1 Merging PLRA time series

In a first step, we merge the PLRA time series. For these missions the topographic sampling by the instruments is similar and thus the offsets are valid over larger regions. For overlapping missions (ERS-1, ERS-2, Envisat, CryoSat-2 LRM) the offsets are calculated from simultaneous epochs (blue area in Fig. 5b), as performed by Wingham et al. (1998) or Paolo et al. (2016). Smoothed grids of these offsets are generated (see Fig. S4) and applied to the respective missions. For the ERS missions, we find significant differences in the offsets for ice and ocean mode, hence, we determine separate offsets for each mode. Comparing our maps with similar maps of offsets between ERS-2 (ice mode) and Envisat shown by Frappart et al. (2016) reveals that the spatial pattern agrees very well but we find significantly smaller amplitudes. We interpret this as a reduced influence of volume scattering due to our low retracking threshold. In accordance with Zwally et al. (2005), we did not find an appropriate functional relationship between the offset and the waveform parameters.

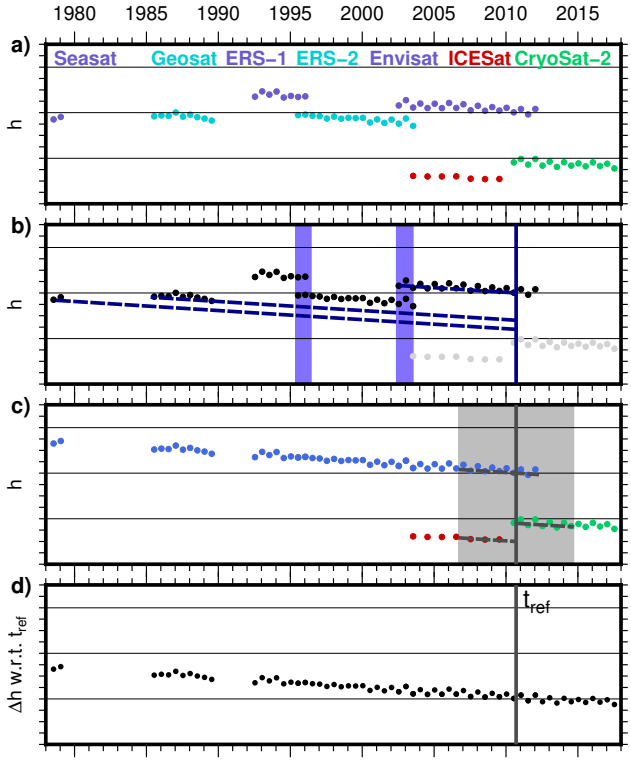

Figure 5. Schematic illustration of the combination of the missions. **a)** Single-mission time series of PLRA missions (blue and cyan), CryoSar-2 in SARIn mode (green) and the laser altimetry measurements of ICESat (red) with inter-mission offsets. **b)** Offsets between the PLRA data are determined from overlapping epochs (blue area) or trend-corrected elevation differences (according to Eq. 2) where dh/dt is sufficiently stable. **c)** The specific offset between PLRA, SARIn and laser data depends on the sampling of the topography within each single cell. These different techniques are aligned by reducing each elevation time series by the specific elevation at the reference epoch t_{ref}. Due to possible non-linear surface elevation changes, this reference elevation is obtained from a 8-year interval only (gray area). **d)** The combined multi-mission time series contains SECs with respect to t_{ref}.

To calibrate Geosat and Seasat, a gap of several years without observations has to be bridged. As depicted by the dashed blue lines in Fig. 5b, we do this using the trend corrected reference elevations $a_{0,M}$ from the joint fit in Eq. (2). This, however, can only be done if the rate is sufficiently stable over the whole period. Therefore, we use two criteria. First, we check the standard deviation of the fit of dh/dt. This $\sigma_{dh/dt}$ indicates the consistency of the observations towards a linear rate during the observational period. However, anomalies during the temporal gaps between the missions (i.e. 1978-1985 and 1989-1992) cannot be detected in this way. Therefore, we furthermore utilize a firn densification model (FDM, Ligtenberg et al., 2011; van Wessem et al., 2018). This model describes the anomalies in elevation due to atmospheric processes against the long-term mean. The RMS of the FDM time series is hence a good measure for the magnitude of the non-linear variations in surface elevation. Consequently, only cells where $\sigma_{dh/dt} < 1\,\mathrm{cm/yr}$ and $RMS_{FDM} < 20\,\mathrm{cm}$, indicating a highly linear rate, are used to calibrate the two historic missions. Maps of the offsets with respect to Envisat are shown in the supplement Fig. S5. Regions

where this stability criterion is fulfilled are mainly found on the plateau. The mean values over all cells amounts to -0.86 m for Seasat and -0.73 m for Geosat. The corresponding standard deviations of 0.85 m and 0.61 m respectively are mainly a result of the regional pattern of the offsets. The true offsets are likely to have spatial variations. However, we are not able to distinguish spatial variations of the offset from residual effects of temporal height variations in the regions meeting the stability criterion. In the regions not meeting this criterion, we are not able to estimate the spatial variations of the offset at all. Therefore, our final estimate of the offset, applied to the measurements, is a constant, calculated as the average offset over the regions meeting the stability criterion. The spatial variability not accounted for by the applied offset is included, instead, in the assessed uncertainty. Our bias between Seasat and Envisat (-0.86±0.85 m) agrees within uncertainties with the ocean-based bias of -0.77 m used by Fricker and Padman (2012). However, we prefer this offset as the observed medium plays an important role for these biases (see Sect. C.3.2 for a more detailed discussion).

With the help of these offsets, all PLRA missions were corrected towards the chosen reference mission Envisat. Uncertainty estimates of the offsets are applied to the respective time series to account for the additional uncertainty. Hence, the PLRA time series are combined (blue in Fig. 5c with additional CryoSat-2 LRM mode where available). At epochs when more than one data set exists, we apply weighted averaging using the uncertainty estimates.

3.3.2 Technique-specific surface elevation changes

In contrast to the PLRA data in the previous step, when merging data from different observation techniques as CryoSat's SARIn mode, ICESat's laser observations and PLRA, also the different sampling of topography has to be considered. As noted in Sect. 3.1 this might lead to completely different surfaces fitted to the respective elevation measurements and thus, the time series need to be calibrated for each cell individually. However, not all cells have valid observations of each data set. Therefore, instead of calibrating the techniques against each other, we reduce each time series by their respective elevation at a common reference epoch and hence obtain time series of surface elevation changes (SEC) w.r.t. this reference epoch instead of absolute elevation time series.

We chose September 2010 as the reference epoch. This epoch is covered by the observational periods of PLRA and CryoSat SARIn and also is exactly one year after the last observations of ICESat, which reduces the influence of an annual cycle. As discussed in Sect. 3.3.1, non-linear elevation changes will adulterate a_0 from Eq. (2), obtained over the full time span. Therefore, we applied another linear fit to a limited time interval of 8 years only (09/2006-09/2014, gray area in Fig. 5c). We subtract the variation of the FDM over this period to account for short-term variations. The limited time interval reduces the influence of changes in ice dynamics. We estimate the individual reference elevations $a_{0,T}$ for each technique T and a joint dh/dt. After subtracting the technique-specific reference elevations $a_{0,T}$ from the respective time series, they all refer to 09/2010 and can be combined.

3.3.3 Merging different techniques

We perform the final combination of the techniques using a weighted spatio-temporal averaging with 10 km σ gaussian weights in spatial domain (up to a radius of 3σ =30 km) and over 3 epochs (i.e. including the two consecutive epochs) in the temporal

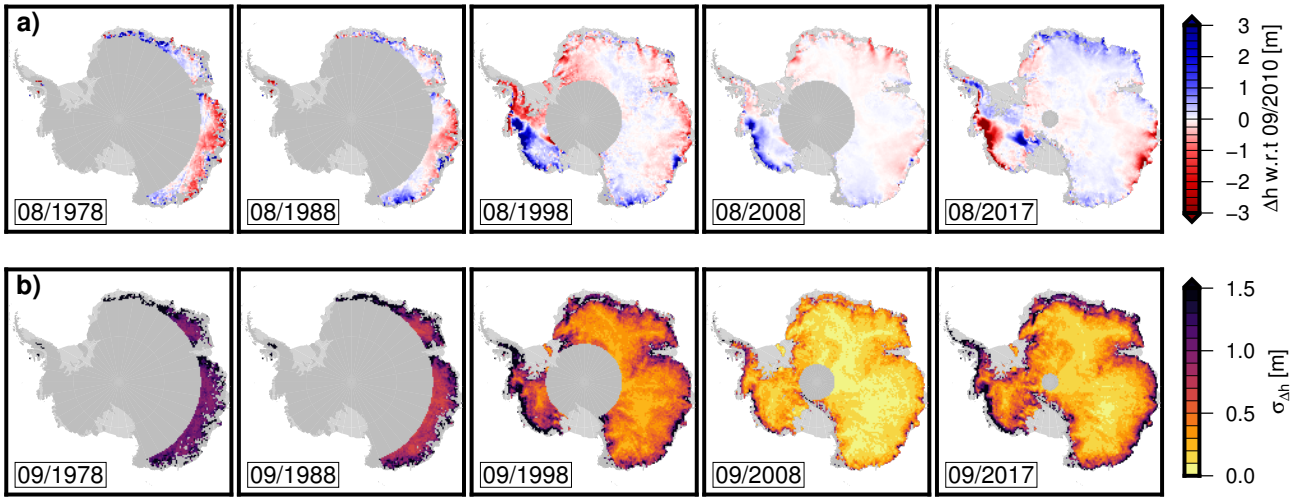

Figure 6. Five example snapshots of the resulting combined surface elevation time series (**a**) and their respective uncertainty (**b**). The height differences refer to our reference epoch 09/2010.

domain. Hence, we obtain grids of surface elevation change (SEC) with respect to 09/2010 for each month observed. Due to the smoothing of the weighting function, we reduce our spatial SEC grid resolution to 10 x10 km. The respective uncertainties are calculated according to the error propagation. To avoid extrapolation and to limit this merging step to the observed area only, we calculate a value for the respective epoch in the 10 x10 km grid cells only if we have data within 20 km around the cells center (which is about the size of a beam-limited radar footprint). The five examples in Fig. 6 demonstrate the spatio-temporal coverage of the resulting SEC grids at different epochs. The respective uncertainty estimates, given in Fig. 6b (further details in the supplement) reach values of one meter and more. Especially in the coastal regions, these uncertainty estimates of our SECs are not defined by the measurement noise and the uncertainty of the offset alone. In regions with fast elevation changes and a large spatial variation in the signal (such as the flow lines of outlet glaciers), the $\sigma_{\Delta h}$ also comprises the variation of the Δh within the area used for smoothing. This holds especially true for epochs that are far away from the reference epoch and, hence, have large values of Δh. Consequently, the epoch 09/2008 provides the lowest uncertainty estimate in these examples, even lower than the CryoSat-2 based epoch 09/2017.

4 Comparison of SEC with independent data

4.1 In situ observations

To validate our results, we used inter-profile crossover differences of 19 kinematic GNSS profiles (Schröder et al., 2017) and elevation differences from Operation IceBridge (OIB ATM L4, Studinger, 2014). The GNSS profiles have been observed between 2001 and 2015 and most of them cover more than 1000 km. One profile (K08C) has not been used as the poorly determined antenna height offset might impose larger errors. For each crossover difference between kinematic profiles from

different years, we compare the differences of the respective altimetric SEC epochs in this location ($\delta\Delta h = \Delta h_{KIN} - \Delta h_{ALT}$). The same analysis has been performed with the elevation changes from OIB. The flights, carried out between 2002 and 2016, were strongly concentrated along the outlet glaciers of West Antarctica and the Antarctic Peninsula. Hence, they cover much more rugged terrain which is more challenging for satellite altimetry. Nevertheless, over the tributaries of the Amundsen Sea glaciers and along the polar gap of ICESat, some repeated measurements have also been performed over flat terrain.

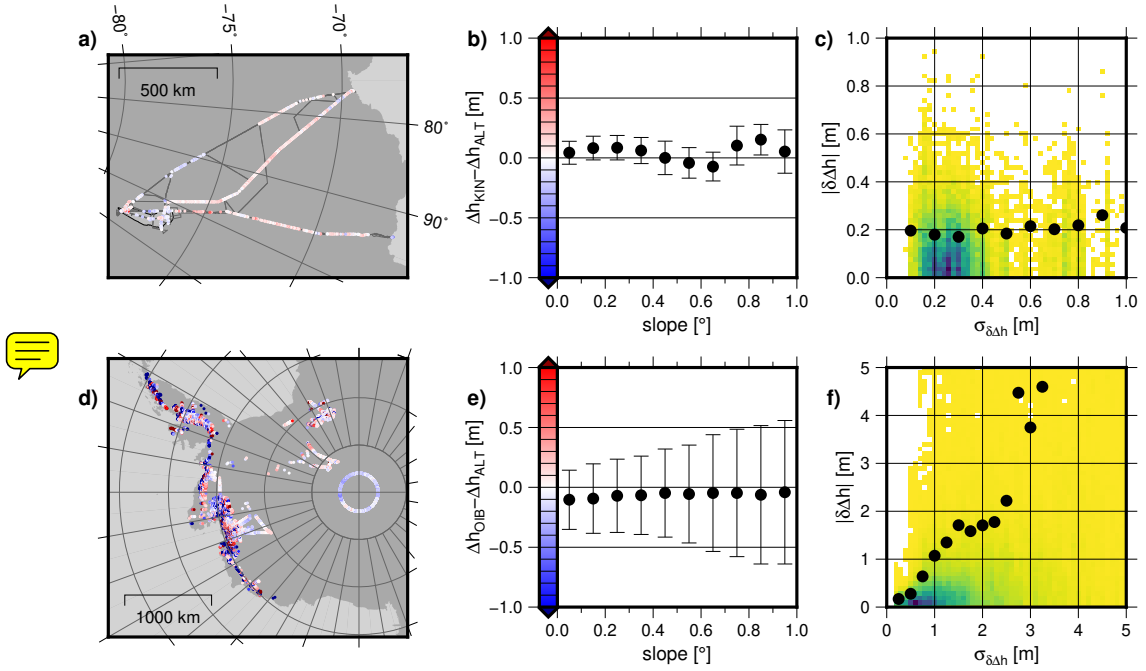

Figure 7. Validation with elevation differences observed by kinematic GNSS (**a,b,c**) and Operation IceBridge (**d,e,f**). Differences between elevation changes observed by the validation data and altimetry are shown on the maps (**a,d**). Median and MAD of these differences, binned by different surface slope, are shown in the center (**b,e**). The right diagrams (**c,f**) show the comparison of these differences with the respective uncertainty estimate, obtained from both data sets. The point density is plotted from yellow to blue and the black dots show the root mean square, binned against the estimated uncertainty.

Figures 7a and d show the results of this validation. A satellite calibration error would lead to systematic biases between the observed elevation differences if Δh_{ALT} is obtained from data of two different missions. However, such biases may also be caused by systematic errors in the validation data. Furthermore, in contrast to the calibration data, the RA measurements may systematically miss out regions which are changing most rapidly if they are located in a local depression (Thomas et al., 2008). With an overall median difference of 6±10 cm for the GNSS profiles and -9±42 cm for OIB, however, the observed elevation changes show only moderate systematic effects and agree within their error bars. The median absolute deviation (MAD) for different specific surface slopes (Fig. 7b and e) reveal the influence of topography in this validation. The GNSS profiles show only a very small increase of this variation with slope. The IceBridge data covers the margins of many West Antarctic glaciers,

where elevation changes differ over relatively short distances. Hence, it is not surprising that we see a significantly larger spread of $\delta\Delta h$ at higher slopes here. However, also for the flat interior, the MAD of the differences is still at a level of 25 cm, which is significantly larger than in the comparison with the GNSS profiles.

The observed $\delta\Delta h$ can further be used to evaluate the uncertainty estimate of the respective elevation differences. In Fig. 7c and f, the uncertainty estimates of the four contributing data are combined and compared to the observed differences. The comparison with both datasets shows that these estimates seem reasonable. In the comparison with the GNSS profiles, the relatively low differences, even in regions which imply a higher uncertainty, are likely just incidental for the small sample of $\delta\Delta h$ along the GNSS profiles.

In conclusion, this validation shows that remaining systematic biases (originating from satellite altimetry or the validation data) are on a centimeter level only and that our uncertainty estimate is realistic. However, we have to stress that only altimetric SEC within the interval 2001-2016 can be validated in this way. For the earlier missions, no spatially extensive high precision in situ data are available to us.

4.2 Firn model

Another data set which covers almost the identical spatial and temporal range as the altimetric data is the firn thickness data set of the IMAU Firn Densification Model (FDM Ligtenberg et al., 2011), forced at the upper boundary by accumulation and temperature of the Regional Atmospheric Climate Model, version 2.3p2 (van Wessem et al., 2018). Before we can compare this model to our SEC results, however, it is important to mention that the FDM only contains elevation anomalies. A long-term elevation trend over 1979-2016, e.g. due to changes in precipitation on longer time scales (Thomas et al., 2015) would not be included in the model. Furthermore, due to the nature of the model, it cannot give information about ice dynamic thinning/thickening. Hence, to compare the FDM and the SEC from altimetry, we first remove a linear trend. This is performed for the period 1992-2016. The trends are only calculated from epochs where both data sets have data, i.e. in the polar gap this comparison is limited to 2003-2016 or 2010-2016, depending on the first altimetry mission providing data here. After the detrending, the anomalies are used to calculate correlation coefficients for each cell, depicted in Fig. 8a. Figure 8b shows the RMS of these anomalies from the altimetry data, representing the magnitude of the seasonal and interannual variations. Comparing the two maps shows that the correlation is around 0.5 or higher, except in regions where the magnitude of the anomalies is small, i.e. where the signal-to-noise ratio of the altimetric data is low. This relationship is depicted in Fig. 8c, where we see that for the vast majority of cells the correlation is positive. For anomalies with a RMS>0.5 m, the average correlation is between 0.3 and 0.6.

Anomalies against the simultaneously observed long-term trend (1992-2016) can also be computed for earlier epochs. Assuming no significant changes in ice dynamics here, these anomalies allow a comparison of Geosat and Seasat with the FDM. The median difference between the anomalies according to Geosat and the anomalies according to the FDM amounts to 0.12±0.21 m (see Fig. S6). Considering that this difference is very sensitive to extrapolating the respective long-term trends, this is a remarkable agreement. With a median of 0.26±0.32 m, the difference between anomalies from Seasat and from the FDM is larger, but this comparison is also more vulnerable to potential errors due to the extrapolation. As the FDM starts in

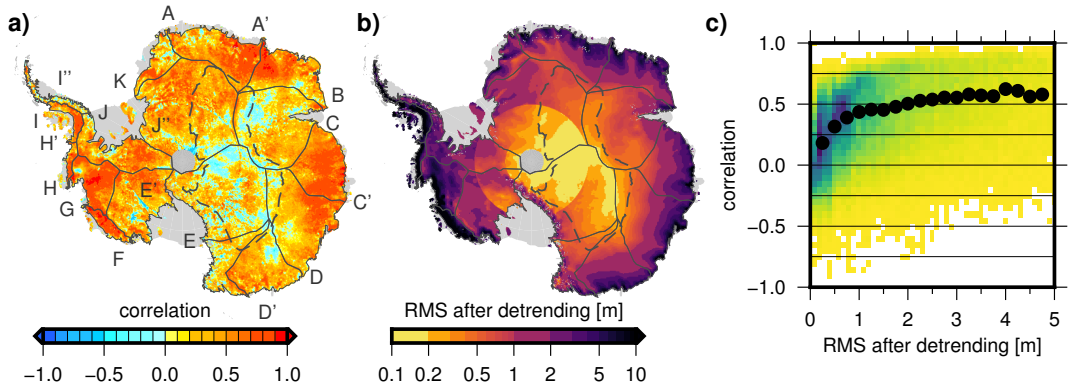

Figure 8. a) Correlation coefficient between the SEC anomalies of the altimetry grids and the FDM over 1992-2016 after detrending. **b)** RMS of the detrended anomalies of the 1992-2016 altimetry time series. **c)** Correlation coefficient plotted against the RMS. The point density is color coded from yellow to blue. The black dots show the binned mean values.

1979 while Seasat operated in 1978, we compare the Seasat data with the FDM anomalies from the respective months of 1979, which might impose additional differences. Finally, the FDM model has its own inherent errors and uncertainties. Therefore, only part of the differences originates from errors in the altimetry results.

5 Results

5.1 Surface elevation changes

Some examples for elevation change time series in the resulting multi-mission SEC grids are shown in Fig. 9 (coordinates in Tab. S2). For Pine Island Glacier (PIG, Fig. 9a), we observe a continuous thinning over the whole observational period since 1992 (Seasat and Geosat measurements do not cover this region). Close to the front (point D) the surface elevation decreased by -45.8±7.8 m since 1992, which means an average SEC rate of -1.80±0.31 $\mathrm{m/yr}$. The time series reveals that this thinning was not constant over time, but accelerated near the grounding line (point D and C at a distance of 40 km) around 2006. Also the points at greater distances from the grounding line (B at 80 km, A at 130 km) show an acceleration around 2006. After 2010, the thinning rates at near front decelerate again. For the period 2013-2017, the rate of -1.3±0.8 $\mathrm{m/yr}$ is very close to the rate preceding the acceleration. In contrast, further inland the thinning did not decelerate so far and is still at a level of about -1.2 $\mathrm{m/yr}$. Hence, for the most recent period (2013-2017) the elevation at all points along the 130 km of the main flow line is decreasing at very similar rates. A similar acceleration near the grounding line, followed by slowdown, is observed by (Konrad et al., 2016). The onset of this acceleration coincides with the detaching of the ice shelf from a pinning point (Rignot et al., 2014). After that speedup terminated around 2009, the grounding line position was relatively stable (Joughin et al., 2016), which agrees with the elevation changes in our observations.

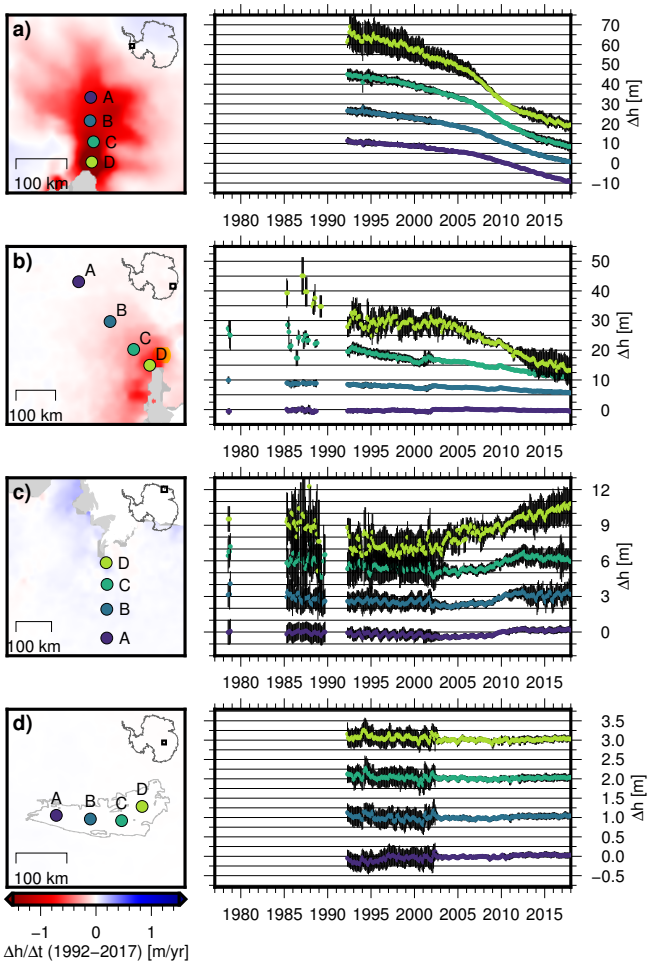

Figure 9. Multi-mission SEC time series in 4 selected regions (**a)** Pine Island Glacier, **b)** Totten Glacier, **c)** Shirase Glacier in Dronning Maud Land and **d)** Lake Vostok). The time series of point B, C and D are shifted along Δh for better visibility. The maps on the left show the elevation change between 1992 and 2017 as in Fig. 10b.

Also for Totten Glacier in East Antarctica (Fig. 9b), we observe a clear negative SEC. This has been previously reported by several authors (e.g. Pritchard et al., 2009; Flament and Rémy, 2012; Zwally et al., 2015) but our data provide an unprecedented time span and resolution. At the very grounding line (point D), Totten Glacier thinned by 31.8±7.7 m between 1987 and 2017, which results in an average SEC rate of -1.0±0.2 m/yr. Seasat could not provide successful observations at the very grounding line but the time series for point C (around 60 km inland) with a rate of -0.38±0.10 m/yr between 1978 and 2017 and for point B (150 km) with a rate of -0.11±0.04 m/yr, respectively, indicate that this thinning already preceded before the epoch of Geosat. At point A in a distance of 280 km, we find no significant elevation change (0.01±0.03 m/yr for 1978-2017). The temporal resolution of these data allows us to analyze the change over time. While we see a significant thinning at the grounding line between 1987 and 1994 of 16.6±9.8 m, the elevation stabilized between 1994 and 2004 to within ±1.5 m. After 2004, the

grounding line thinned again by 15.4±5.5 m until 2017. Li et al. (2016) observe a similar variation in ice velocity measurements between 1989 and 2015. Combining their ice discharge estimates with surface mass balance, they obtain a relatively large mass imbalance for Totten Glacier in 1989, decreasing in the following years to a state close to equilibrium around 2000. After 2000, they observe an acceleration of ice flow, again consistent with our thinning rates. The authors attribute this high variability to variations in ocean temperature. In another study, Li et al. (2015) observe a grounding line retreat at Totten Glacier of 1 to 3 km between 1996 and 2013 using SAR Interferometry. They conclude that this indicates a thinning by 12 m, which is again consistent with our results over this period (12.0±8.8 m).

At Shirase Glacier in Dronning Maud Land (DML, Fig. 9c), we observe a relatively stable surface with a slightly negative change rate between 1978 and the early 2000s. In this region, two significantly positive accumulation anomalies occurred in 2009 and 2011 (Boening et al., 2012; Lenaerts et al., 2013). The increase in surface elevation associated to these event is visible in our time series. At point C, the elevation changed by 1.0±1.5 m between 2008 and 2012. Even at point A, more than 200 km inland and at an altitude of 2500 m, the elevation increased by 0.55±0.50 m during this time. At point D, a similar jump is observed in 2003, which corresponds to another SMB anomaly (cf. Fig. 2a in Lenaerts et al., 2013).

In contrast to the regions discussed so far, the elevation change on the plateau of East Antarctica is very small. The time series for four different points at Lake Vostok (Fig. 9d) show rates which are very close to zero (point A: 5±9 mm/yr, B: -1±10 mm/yr, C: -3±9 mm/yr, D: -1±10 mm/yr between 1992 and 2017). The larger variations in the ERS time series is a result of the lower resolution of the waveform in the ice mode of the ERS satellites. These rates contradict the findings of Zwally et al. (2015). They report a surface elevation increase of 20 mm/yr over Lake Vostok, which would result in an increase of elevation of 0.5 m over the period 1992-2017. Our results are confirmed by ground based static GNSS observations (Richter et al., 2008, 0.3±4.9 mm/yr), kinematic GNSS profiles measured around Vostok Station using snow mobiles (Richter et al., 2014, 1±5 mm/yr) and by GNSS profiles using traverse vehicles over the entire Lake Vostok region (Schröder et al., 2017, -1±5 mm/yr).

The full pattern of surface elevation changes is shown in Fig. 10. These change rates are obtained by calculating elevation differences between the respective years, divided by the time difference. To reduce remaining noise, we use yearly averages (January-December). If one of the years does not cover the full annual cycle, we calculate the average only from the months covered in both years (July-October for 1978-2017, April-December for 1992-2017). We calculate the SEC rate from epoch differences instead of fitting a rate to all epochs because the first observations at specific latitudes start in different years, the observations have different precisions and the large gap between 1978 and 1985 is not covered by observations at all. These three points would lead to a bias towards the later epochs in a fit, which would not be representative for the true average elevation change over the full interval.

The long-term elevation changes over 25 years (Fig. 10b) show the well known thinning in the Amundsen Sea Embayment and at Totten Glacier, as well as the thickening of Kamb Ice Stream (cf. e.g. Wingham et al., 2006b; Flament and Rémy, 2012; Helm et al., 2014). In contrast, 60% of East Antarctica north of 81.5°S shows surface elevation changes of less than ±1 cm/yr. However, several coastal regions of the EAIS show significant elevation changes, too. Totten Glacier (T in Fig. 10b) is thinning at an average rate of 72±18 cm/yr at the grounding line (cf. Fig. 9b). Several smaller glaciers in Wilkes Land also

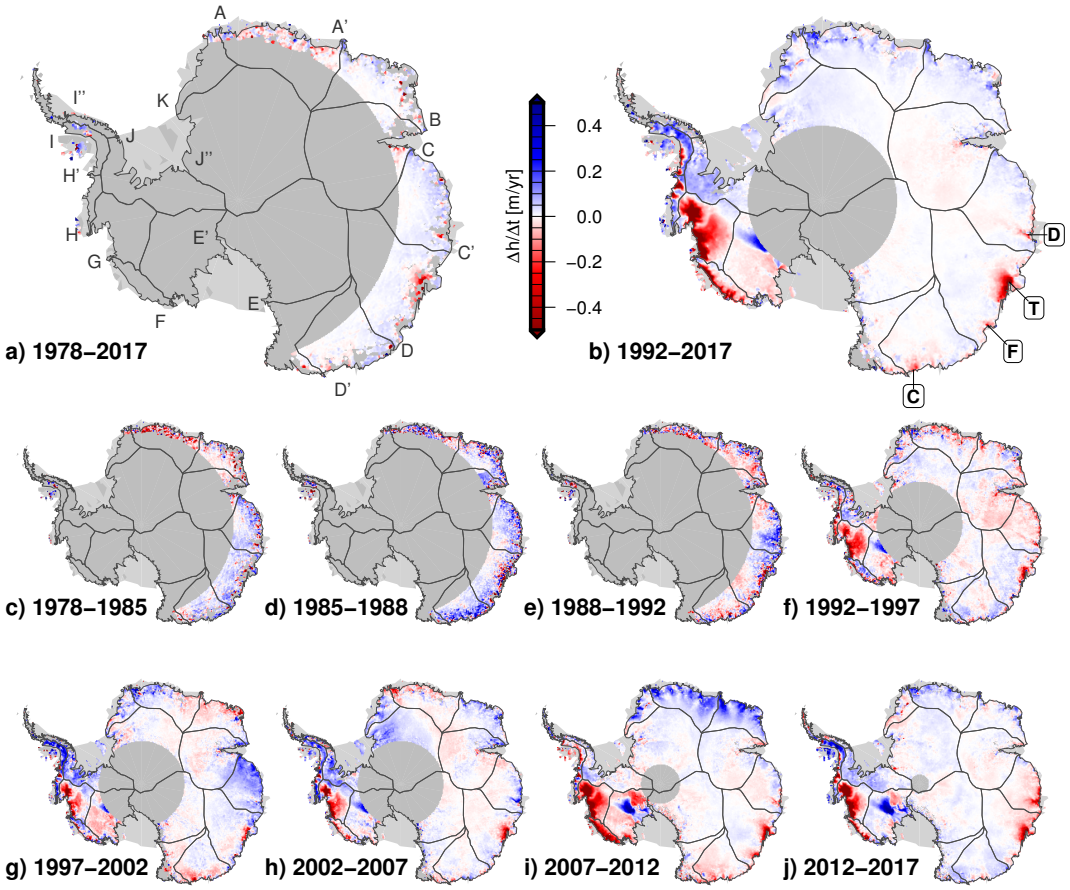

Figure 10. Multi-mission surface elevation change from the combined SEC time series over different time intervals. **a** and **b)** The long-term surface elevation change between 1978 and 2017 and 1992 and 2017 for the respectively covered area. **c-j)** Elevation change over consecutive time intervals reveal the interannual variability. Thin lines mark the drainage basin outlines, denoted in **a**. Bold letters in boxes in **b** denote glaciers, mentioned in the text.

a persistent thinning. We observe SEC rates of -26±10 $\mathrm{cm/yr}$ at Denman Glacier (D), -41±19 $\mathrm{cm/yr}$ at Frost Glacier (F) and -33±12 $\mathrm{cm/yr}$ near Cook Ice Shelf. Rignot (2006) showed that the flow velocity of these glaciers, which are grounded well below sea level, was above the balance velocity for many years. In contrast, the western sector of the EAIS (Coats Land, DML and Enderby Land, basins J''-B) shows thickening over the last 25 years at rates of up to a decimeter per year.

Comparing the long-term elevation changes over 40 years (Fig. 10a) with those over 25 years shows the limitations of the early observations, but also the additional information they provide. There were only relatively few successful observations at the very margins but e.g. for Totten or Denman Glacier, they show similar rates at a distance of about 100 km from the grounding line. In DML and Enderby Land (basins A-B in Fig. 10a), the 40 yr interval shows less positive rates, compared to 1992-2017. Until 2002, a large part of this region even experienced significant thinning (see time series in Fig. 9c and the

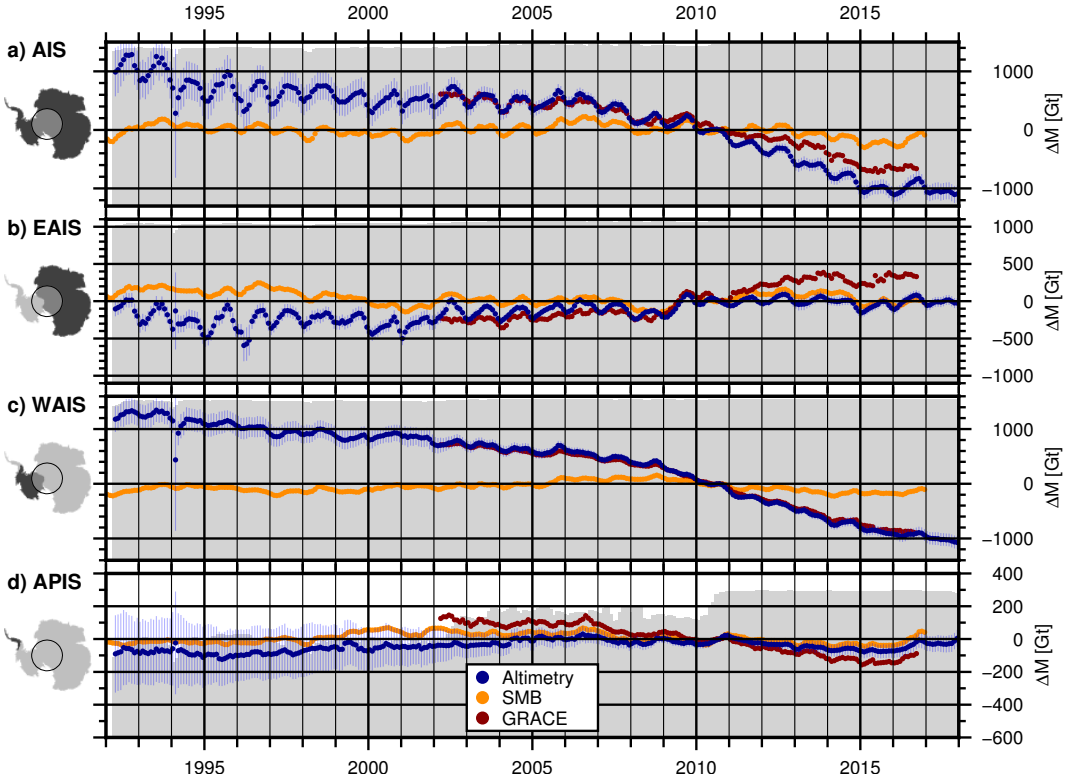

Figure 11. Mass change of the Antarctic Ice Sheet north of 81.5°S (**a**) and the three subregions (**b** EAIS, **c** WAIS and **d** APIS) from our combined altimetric time series (blue), GRACE (red) and SMB (orange). The error bars show the uncertainty estimate σ_Σ of the altimetry data according to Sect. F.2. The gray color in the background displays the fraction of the area covered by altimetry (up to the top means 100%).

maps for the sub-intervals in Fig. 10c-g). After that time, especially over the period 2007-2012 (Fig. 10i), this region shows a huge increase in elevation, which relates mainly to the accumulation events in 2009 and 2011. The sub-intervals in Fig. 10c-j demonstrate the effect of interannual snowfall variability on the elevation change rates over shorter time intervals. They show similar variations also in other regions, pointing out that accumulation events have a strong influence on interannual elevation changes over all parts of Antarctica (Horwath et al., 2012; Mémin et al., 2015).

5.2 Ice sheet mass time series

In order to determine the effect of the SEC on global sea level, they are converted to ice mass changes. In a first step, all time series are corrected for glacial isostatic adjustment (GIA) using the IJ05_R2 model (Ivins et al., 2013). This GIA model predicts an uplift of $5\,\mathrm{mm/yr}$ near the Antarctic Peninsula and rates between -0.5 and $+2\,\mathrm{mm/yr}$ in East Antarctica. Furthermore we applied a scaling factor $\alpha = 1.0205$ to account for elastic solid earth rebound effects (Groh et al., 2012). We multiply the resulting ice sheet thickness changes by each cell's area and apply a density according to a firn/ice mask (McMillan et al., 2014,

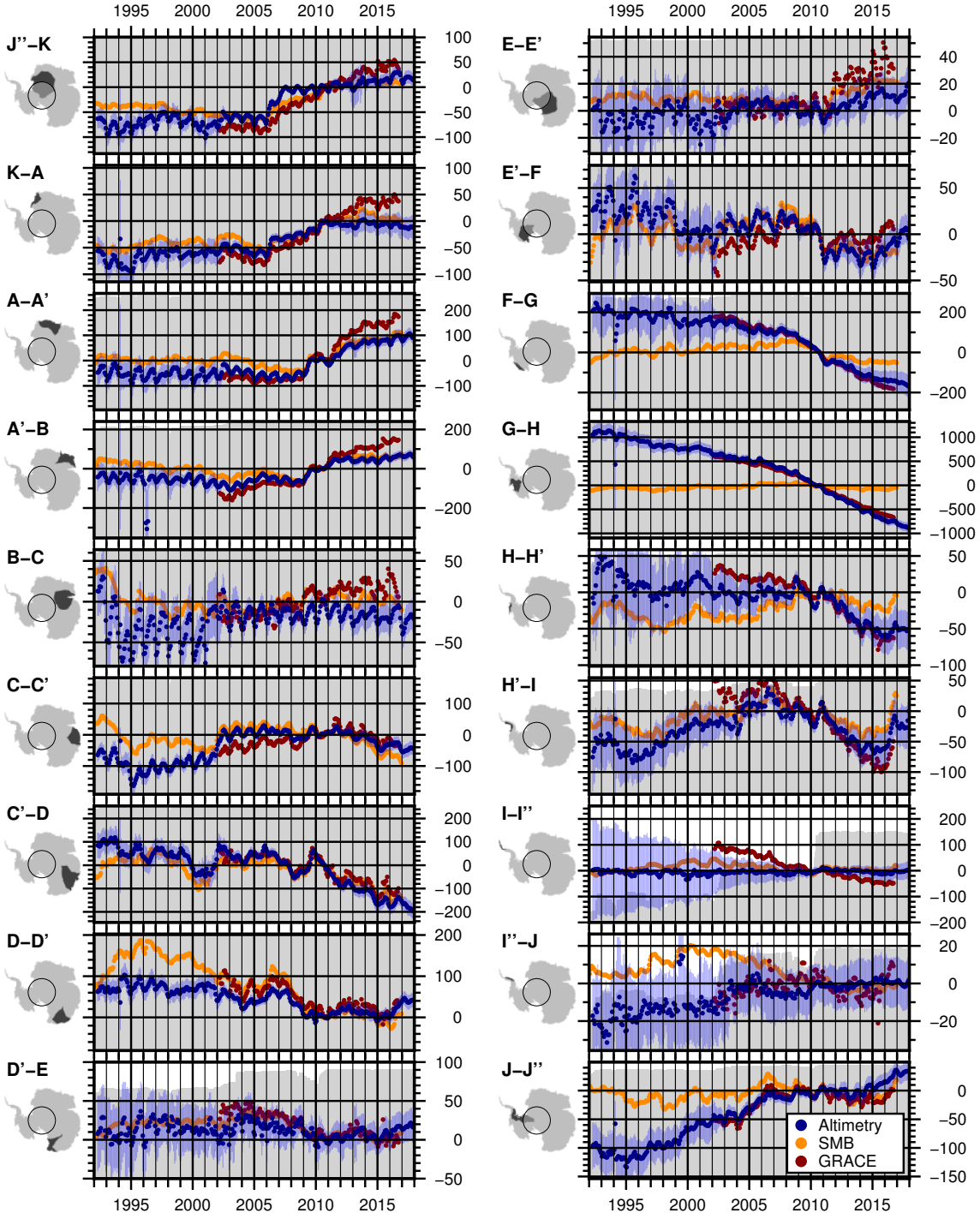

Figure 12. Mass change ($\Delta M[Gt]$) of the individual drainage basins north of 81.5°S from our combined altimetric time series (blue), GRACE (red) and SMB (orange). The error bars show the uncertainty estimate σ_Σ of the altimetry data according to Sect. F.2. The gray color in the background displays the fraction of the area covered by altimetry (up to the top means 100%).

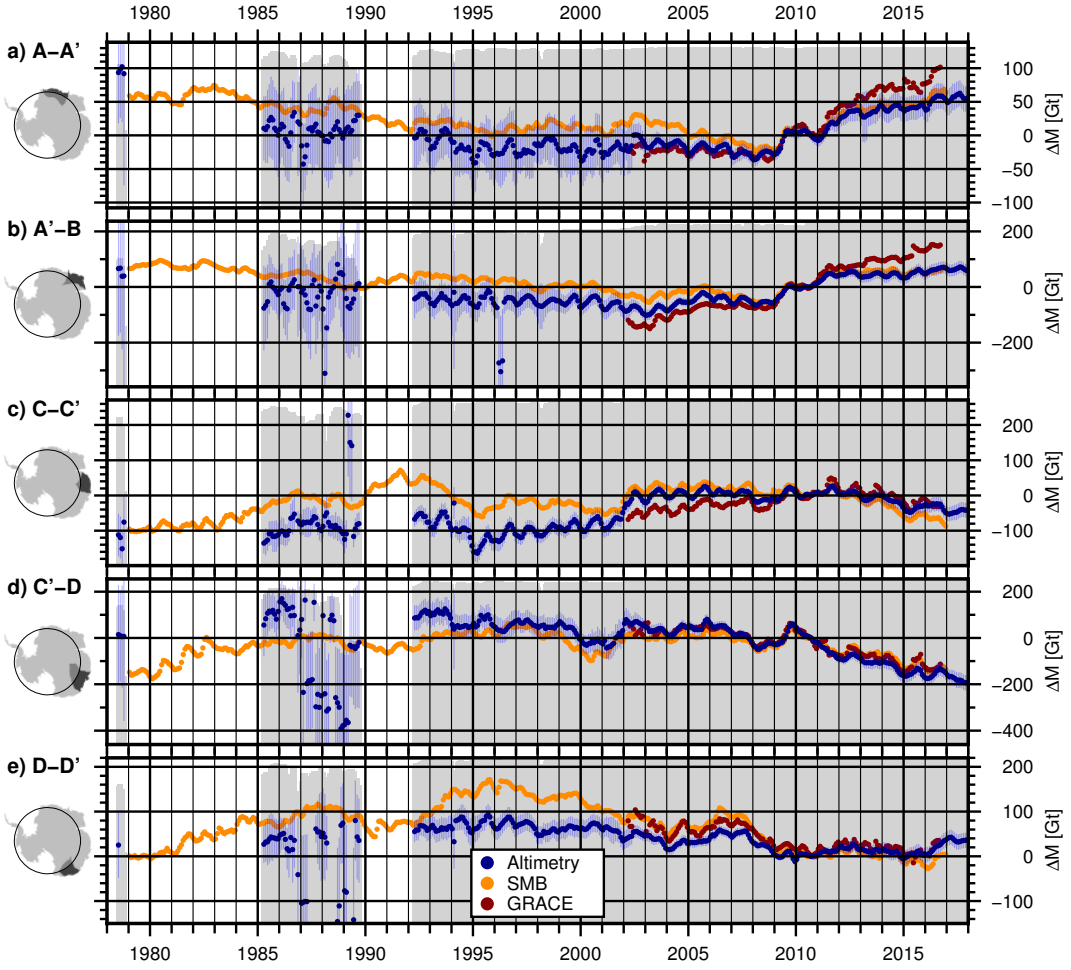

Figure 13. Mass change of subregions north of 72°S for several East Antarctic drainage basins from our combined altimetric time series (blue), GRACE (red) and SMB (orange). The error bars show the uncertainty estimate σ_Σ of the altimetry data according to Sect. F.2. The gray color in the background displays the fraction of the area covered by altimetry (up to the top means 100%).

2016), depicted in Fig. S8, to obtain a mass change. In regions where ice dynamic processes are assumed to be dominating (e.g. in Amundsen Sea Embayment, Kamb Ice Stream or Totten Glacier), we use a density of 917 $\mathrm{kg/m^3}$. Elsewhere, we apply the density of near-surface firn, obtained from firn modeling using atmospheric forcing (Ligtenberg et al., 2011). We have chosen this straightforward and robust method here, instead of using modeled temporal variations of the firn layer (as e.g. Zwally et al., 2015; Kallenberg et al., 2017) in the volume-to mass conversion. This allows us to compare the time series from altimetry with time series from SMB modeling.

Cumulated mass anomalies over larger regions such as drainage basins or even the total AIS are obtained by summing up the results accordingly. Therefore, we used the basin definitions by Rignot et al. (2011) (updated for Shepherd et al. (2018), see Figs. 10a and 14b). Cells containing no valid data after the gridding (as e.g. where not enough observations were available,

in the polar gap or where rocks are predominant) are not considered here. Uncertainty estimates were obtained by propagating the respective uncertainties of the SEC, the GIA and the firn density to the basin sums for each month (see Sect. F.2 for details). We also include an estimate for the effect of unobserved cells in the error budget.

Figures 11a-d show time series for the entire AIS north of 81.5°S (i.e. covered by satellite altimetry since 1992), and the respective subregions EAIS, WAIS and the APIS. Similar time series for the single drainage basins over 1992-2017 are shown in Fig. 12. The full four decade time interval for the coastal areas of the EAIS is shown in Fig. 13. These time series use the data north of 72°S only and, hence, provide a nearly consistent observational coverage since 1978. To support the interpretation and evaluate the temporal evolution, we compared the respective time series to GIA-corrected cumulated mass anomalies from satellite gravimetry (GRACE, Groh and Horwath, 2016). To reduce the effect of noise in the GRACE monthly solutions and to make the data more comparable to our altimetry results, we applied a three-month moving average to the GRACE time series. We also compare our data to time series of cumulated surface mass balance anomalies from RACMO2.3p2 (SMB, van Wessem et al., 2018). Similar to the firn model, the SMB contains seasonal and interannual variations due to surface processes. However, it assumes an equilibrium over the modeled period and, hence, does not include long-term changes. The different time series show the good agreement of the techniques in resolving interannual variations. For example for the basin of Totten Glacier (C'-D in Fig. 12), all techniques observe a negative mass anomaly in early 2008, followed by a significant mass gain in 2009. Between 03/2008 and 10/2009, we obtain a mass difference of 116.6±27.0 Gt from altimetry, 109.4 Gt from SMB and 113.4 Gt from GRACE. The high agreement with the SMB indicates that this mass gain is caused by snow accumulation. In most of the basins, we observe similar high agreement in the short-term variations. A good example for the different components of the total mass change signal is the Getz and Abbot region (F-G). While all techniques observe a significant mass loss between 2009 and 2011, the SMB does not contain a long term trend, as observed by altimetry and GRACE. In some regions, however, there are also significant discrepancies between the different data sets. The poor sampling of the northernmost APIS (I-I") by altimetry is a good example for the limitations of this technique. In George V Land (D-D'), the agreement during the GRACE period is reasonable, while the mass gain, indicated by the SMB in the early 1990s is not revealed by the altimetry time series.

Over the last 25 years our data indicate a clearly negative mass balance of -2068±377 Gt for the AIS (Fig. 11a). This is mainly a result of the mass loss in the WAIS over the last decade. In contrast, the EAIS has been very stable over our observational record (120±121 Gt between 1992 and 2017). The time series of the APIS contains large uncertainties due to many unobserved cells. Mass change rates for selected regions, obtained from the differences over a specific time interval, and their respective uncertainties are given in Tab. 2. We calculated separate trends for the area north of 72°S, which is covered by all satellites, north of 81.5°S which is covered since ERS-1 and for the total area, which is (except the 500 km diameter polar gap) covered since CryoSat-2. The observed area shows that 96.4% of the cells, classified as ice sheet north of 81.5°S, are successfully covered by observations of ERS-1. Cells without successful observation occur mostly at the APIS, where only 61% is covered with data.

From the overall mass loss of -2068±377 Gt for the AIS (<81.5°S over 1992-2017) we obtain an average long-term rate of -84.7±15.5 Gt/yr. This rate agrees within error bars but is considerably smaller than the results of Shepherd et al. (2018) of -109±56 Gt/yr. However, the extended material in Shepherd et al. (2018) shows that there are still some discrepancies

Table 2. Mass change rates for different regions of the Antarctic Ice Sheet and different time intervals. The sizes of the total and observed area refer to all cells classified as ice sheet in the respective region (and, if stated, limited by the given latitude).

region	area [$10^3 \mathrm{km}^2$]		dM/dt [$\mathrm{Gt/yr}$]				
	total	observed	1978-2017	1992-2017	1978-1992	1992-2010	2010-2017
AIS	11892	11630	-	-	-	-	-117.5±25.5
EAIS	9620	9413	-	-	-	-	1.6±13.1
WAIS	2038	2008	-	-	-	-	-114.5±19.9
APIS	232	208	-	-	-	-	-4.5±8.7
AIS (<81.5°S)	9391	9053	-	-84.7±15.5	-	-58.6±20.3	-137.0±24.9
EAIS (<81.5°S)	7764	7555	-	4.9±5.0	-	8.0±6.2	2.4±12.4
WAIS (<81.5°S)	1394	1358	-	-91.7±10.3	-	-69.4±13.1	-134.9±19.6
APIS (<81.5°S)	232	142	-	2.1±8.9	-	2.8±12.3	-4.5±8.7
EAIS (<72°S)	2779	2274	1.5±5.8	-3.4±4.0	12.1±17.4	0.0±4.9	-8.4±10.1

For the APIS (<72°S), the very sparse observations of Seasat and Geosat did not allow calculate a reliable trend.

between the different techniques to determine the AIS mass balance. For the time interval 2003-2010 (Extended Data Table 4 in Shepherd et al., 2018) the Input-Output method obtains a rate of -201±82 $\mathrm{Gt/yr}$ for the AIS, while the mass balance rates, aggregated from satellite gravimetry (-76±20 $\mathrm{Gt/yr}$) and from altimetry (-43±21 $\mathrm{Gt/yr}$) agree much better with our result for the AIS (<81.5°S) between 2003 and 2010 of -64.7±24.9 $\mathrm{Gt/yr}$.

6 Discussion

6.1 Multi-mission SEC time series

The single-mission time series, obtained in Sect. 3.2, contain satellite-specific calibration biases as well as offsets due to the specific sampling characteristics of different sensor types. In order to form a consistent SEC time series, these biases needed to be determined and corrected. A comparison with in situ data showed that there are no significant offsets between elevation changes from our multi-mission altimetry data and the validation datasets. This comparison, however, could only validate our data in the interval 2001-2016. A quality control for the whole time span was performed by a comparison with a firn model. The correlation of the detrended data sets shows that especially for regions where the interannual variation is large (compared to the measurement noise of the altimeters) both time series agree very well. This comparison even provided independent estimates for the error of the early missions. The average differences between the detrended time series of the FDM and the SEC show that the observations of Geosat and even of Seasat agree with the model results within a few decimeters. For SECs of up to several meters w.r.t 2010 (see Fig. 6), this means that also the older data can be used to calculate elevation change rates with an accuracy better than a centimeter per year (see Fig. S7a). Unfortunately, in coastal DML west of the ice divide A', the data of

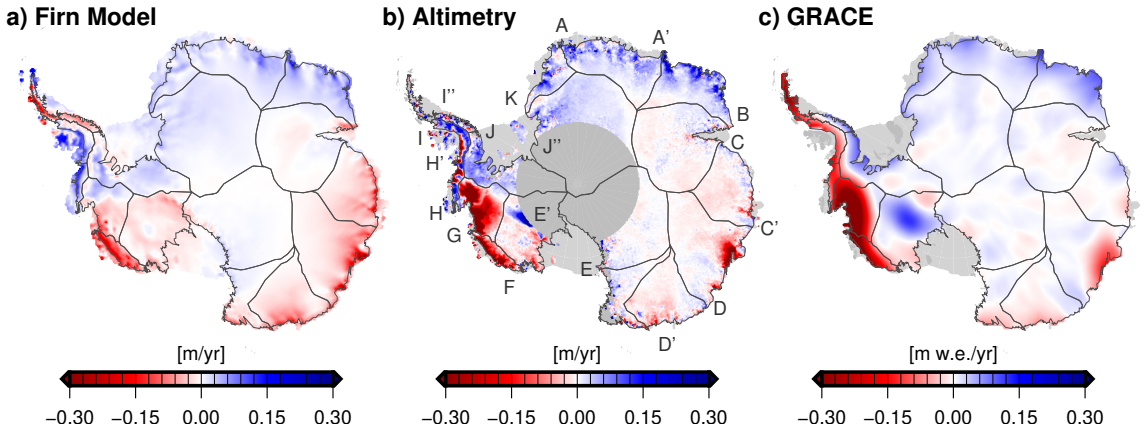

Figure 14. Mean rates for the time interval 2002-2016 of elevation changes from IMAU-FDM **(a)**, from the multi-mission SEC grids **(b)** and of the mass changes from GRACE **(c)**.

Seasat and Geosat are very noisy. This due to the mountain ranges just north of 72°S, which lead to many losses of lock of the measurements all the way across this part of the ice sheet. The same applies to the measurements at the APIS.

6.2 Surface elevation changes

The mean rates of elevation change in Fig. 10 show the regions which experience a significant thinning (Amundsen Sea Embayment, Totten Glacier) or thickening (Kamb Ice Stream) which was already reported by previous publications (e.g. Wingham et al., 2006b; Flament and Rémy, 2012; Helm et al., 2014; Zwally et al., 2015). By combining all the single missions consistently we analyze long-term changes over the full time period covered. For 79% of the area of the AIS, this means a time span of 25 years. For 25%, mainly the coastal regions of East Antarctica, even 40 years are covered. We assume that these long-term trends are significantly less affected by short-term variations in snowfall than a trend from a single mission.

The benefits of a seamless combination of the time series are demonstrated in Fig. 10. The time intervals for the elevation changes are independent of the observational period of a single mission. This is necessary to analyze processes which occurred close to the transition between different missions. A good example of the advantage of such long time series are the elevation changes caused by the accumulation events in DML. Figure 9c clearly shows the changes in elevation, caused by the strong snowfall events in 2009 and 2011. The mission lifetime of ICESat ended in 10/2009, CryoSat-2 provided the first measurements in 07/2010. Only Envisat covered both events but here, the orbit was shifted in 10/2010, resulting in different repeat track cells covered before and after the orbit shift. We merged all these missions as described in Sect. 3.3, which allows us to analyze the full time series. Comparing the elevation change from altimetry e.g. at point A in Fig.9c of 0.55±0.50 m with the change modeled using the FDM (0.48 m between 2008 and 2012) is a good example of successfully cross-validating these two data sets. Figure 8 shows the degree of agreement over the entire AIS.

As these elevation change rates alone do not contain any information on their origin, additional data are needed for improved process understanding. Figure 14 shows SEC rates for the interval 2002-2016 (March-September respectively) from altimetry and the FDM and respective rates of ice mass changes from GRACE. These maps show that the elevation gains in DML and Enderby Land agree very well with the firn model, which implies that increased snow accumulation during this period is responsible for the thickening. For Princess Elizabeth Land (C-C'), the negative rates agree as well, implying that the thinning here can be related to lower than normal snow accumulation. In contrast, the strong thinning along the Amundsen Sea Embayment (G-H) or the thickening of Kamb Ice Stream (E'-F) is not present in the FDM results but does show up in the GRACE data. Due to the higher densities of the involved material, ice dynamic processes show up even more pronounced in the map of mass changes, compared to the maps of elevation changes.

The inland propagation of dynamic thinning of the glaciers of the Amundsen Sea Embayment over the last decades has been described by Konrad et al. (2016). A recent onset of significant mass losses has also been reported for the adjacent glaciers along the Bellingshausen Sea (H-I, Wouters et al., 2015) and in the Getz and Abbot region (F-G, Chuter et al., 2017). Fig. 10i reveals that the largest losses along the coast of the WAIS occurred between 2007 and 2012. The period 2012-2017 (Fig. 10i) shows that only a part of these large rates is persistent, indicating that also interannual variations in SMB have to be considered here (see also Chuter et al., 2017). The FDM-derived rate in Fig. 14a confirms the role of the surface mass balance in this region.

6.3 Ice sheet mass time series

The individual basin time series for these regions of the WAIS (in Fig. 12) allow us to analyze the increasing losses at a monthly resolution. They show that in 2004, the thinning of the Getz and Abbot region accelerated and experienced a further acceleration after 2007. After a small positive mass anomaly in late 2005, which relates to a similar event in the SMB time series, the overall mass losses in the Amundsen Sea Embayment accelerated. The Bellingshausen Sea basin was relatively stable until 2009, but started to lose significant amounts of mass after that time, as reported by Wouters et al. (2015). Since this study, however, we observe that the basins at the western part of the Peninsula (H-I) regained mass. The comparison with SMB reveals that this can be explained by a positive snowfall anomaly in this area in 2016. The shape and orientation of the Peninsula makes GRACE observations challenging with respect to leakage and GRACE error effects (Horwath and Dietrich, 2009). Nevertheless, the results of the satellite gravity mission confirm this mass anomaly.

The comparison of the ice sheet wide mass time series between altimetry and GRACE in Fig. 11 reveals that for the WAIS, both datasets agree very well, while for the APIS and the EAIS, significant differences are found. The percentage of observed area of the APIS (gray area in the background of Fig. 11d) indicates that before 2010 a significant part of the area remained unobserved. Here, conventional RA measurements very often failed due to the rugged terrain. Even for ICESat, the large across track distances and the dependence on cloud-free conditions make measurements very sparse here. With the weather independent, dense and small footprint measurements of CryoSat-2 in SARIn mode, up to 80% of the area are covered by observations. Compared to GRACE, however, we observe a significantly weaker mass loss signal. Thomas et al. (2008) pointed out that RA fails to sample especially the large elevation changes in narrow valleys of outlet glaciers. This leads to an overall

underestimation of the signal by altimetric observations. Even for ICESat this is true in this case, as cloudy conditions are not unusual in this region. But even when enough valid measurements would have been available, the fit of a planar surface over a diameter of 2 km would have been very challenging in the initial repeat altimetry processing here. Our approach is designed to provide valid observations over the majority of the AIS. Under the challenging conditions of the APIS, modifications such as a smaller diameter or more complex parametrization of the surface would surely help to improve the results. Furthermore, we did not calculate a SEC for cells that are further away than a beam-limited radar footprint from valid measurements. In order to interpolate or even extrapolate the results to unobserved cells, advanced gridding methods such as kriging, especially with the help of additional data sets (Hurkmans et al., 2012), would be advisable. In contrast, here we concentrate on the observed cells only.

For the EAIS (Fig. 11b) we see significant differences between the time series of mass changes from altimetry and from GRACE. For the time interval 2002 to 2016 (see Sect. F.3), the mean rate from altimetry (9.6±6.9 $\mathrm{Gt/yr}$) is mainly dominated by the accumulation events in 2009 and 2011. In contrast, the GRACE data imply an average mass gain of 42.1 $\mathrm{Gt/yr}$ over this time interval. Especially after 2011, the differences become very prominent in the time series. The respective mass changes for the individual basins (Fig. 12) reveal that this difference in the signals can be attributed to DML and Enderby Land. This might be a sign for dynamic thickening. Here, all elevation changes have been converted to mass using the density of surface firn. If a part of the positive elevation changes in this region indeed would be caused by ice dynamics, this would lead to an underestimation of mass gains from altimetry compared to gravimetric measurements. The results of the Bayesian combined approach of Martín-Español et al. (2017) also suggest a small dynamic thickening in this region. Rignot et al. (2008) observed no significant mass changes in this region between 1992 and 2006 using the input-output-method. Gardner et al. (2018) compared present day ice flow velocities to measurements from 2008. They obtain a slightly reduced ice discharge in DML (which would support the hypothesis of a dynamic thickening), while they observe a small increase in discharge for Enderby Land. Part of this misfit might also be explained by remaining processing issues in the GRACE processing (e.g. the GIA correction). Hence, we conclude that further work is needed to identify the origin of this discrepancy.

7 Conclusions

In this paper we presented an approach to combine different satellite altimetry missions, observation modes and techniques. The reprocessing of the conventional pulse limited radar altimetry ensures that two fundamental steps in processing of radar ice altimetry, the waveform retracking and the slope correction, are performed consistently. Furthermore, we showed that the advanced methods, used in this processing, improved the precision by more than 50%, compared to the widely used standard products. The validation with in situ measurements and the comparison with the IMAU-FDM shows that inter-mission offsets have been successfully corrected and that the uncertainty estimates for our resulting monthly multi-mission SEC grids are realistic.

We analyzed the resulting time series and found that they provide detailed insight in the evolution of the surface elevation of the Antarctic Ice Sheet. From the combined SEC time series we calculated the long-term surface elevation change over the

last 25 years. Due to Seasat and Geosat, observations in the coastal EAIS date back until 1978, covering four decades. The unique data show that large parts of the East Antarctic plateau are very close to equilibrium, while changes over shorter time intervals identify interannual variations, which cannot be identified in long-term trends and are mostly associated with snowfall anomalies.

The monthly mass time series show that the AIS (excluding the polar gap within 81.5°S) lost an average amount of mass of -84.7±15.5 $\mathrm{Gt/yr}$ between 1992 and 2017. These losses accelerated in several regions and, hence, for 2010-2017 we obtain -137.0±24.9 $\mathrm{Gt/yr}$ for the same area. The comparison of the altimetry-derived mass changes, integrated over different basins and regions of the ice sheet, with SMB and GRACE shows high consistency of the different techniques. A correlation coefficient between the mass anomalies from altimetry and from GRACE of 0.96 (for the time interval 2002-2016, see Tab. S4) indicates the excellent agreement of the observed interannual variations. The respective correlation with the SMB anomalies (0.60 for 1992-2016) is comparatively lower but still indicates a high agreement. In the APIS, differences between the mass time series of the different techniques arise mainly due to the poor spatial sampling of the altimetry data, while for the EAIS, the remaining discrepancies to mass time series from GRACE might be explained by the density mask used. These remaining issues and open questions should be addressed in future work in order to further reduce the uncertainty of the estimates of the mass balance of the AIS. The recently launched laser altimeter ICESat-2 promises a new milestone in ice sheet altimetry. We believe that our multi-mission combination approach can provide an important tool to combine the extremely high resolution of this mission with the long time period, covered by the previous missions.

Author contributions. L. Schröder designed the study and developed the PLRA reprocessing, the repeat altimetry processing and the time series generation. V. Helm supplied the reprocessed CryoSat-2 SARIn data. Stefan Ligtenberg and Michiel van den Broeke provided the RACMO and IMAU-FDM models. All authors discussed the results and contributed to the writing and editing of the manuscript.

Acknowledgements. This work is supported by the Deutsche Bundesstiftung Umwelt (DBU, German Federal Environmental Foundation). We thank the European Space Agency, the National Snow and Ice Data Center and the NASA Goddard Space Flight Center for providing the altimetry data products. Especially we would like to thank Jairo Santana for his support to access the GSFC data.

References

Arthern, R., Wingham, D., and Ridout, A.: Controls on ERS altimeter measurements over ice sheets: Footprint-scale topography, backscatter fluctuations, and the dependence of microwave penetration depth on satellite orientation, Journal of Geophysical Research – Atmospheres, 106, 33 471–33 484, 2001.

Bamber, J.: Ice Sheet Altimeter Processing Scheme, Int. J. Remote Sensing, 14, 925–938, 1994.

Bamber, J., Gomez-Dans, J., and Griggs, J.: A new 1 km digital elevation model of the Antarctic derived from combined satellite radar and laser data – Part 1: Data and methods, The Cryosphere, 3, 101–111, https://doi.org/10.5194/tc-3-101-2009, 2009.

Boening, C., Lebsock, M., Landerer, F., and Stephens, G.: Snowfall-driven mass change on the East Antarctic ice sheet, Geophys. Res. Lett., 39, L21 501, https://doi.org/10.1029/2012GL053316, 2012.

Brenner, A., Bindschadler, R., Zwally, H., and Thomas, R.: Slope-induced errors in radar altimetry over continental ice sheets, J. Geophys. Res., 88, 1617–1623, https://doi.org/10.1029/JC088iC03p01617, 1983.

Brenner, A., DiMarzio, J., and Zwally, H.: Precision and Accuracy of Satellite Radar and Laser Altimeter Data Over the Continental Ice Sheets, IEEE Trans. Geosci. Remote Sens., 45, 321–331, https://doi.org/10.1109/TGRS.2006.887172, 2007.

Brockley, D., Baker, S., Femenias, P., Martinez, B., Massmann, F.-H., Otten, M., Paul, F., Picard, B., Prandi, P., Roca, M., Rudenko, S., Scharroo, R., and Visser, P.: REAPER: Reprocessing 12 Years of ERS-1 and ERS-2 Altimeters and Microwave Radiometer Data, IEEE Trans. Geosci. Remote Sens., 55, 5506–5514, https://doi.org/10.1109/TGRS.2017.2709343, 2017.

Chuter, S., Martín-Español, A., Wouters, B., and Bamber, J.: Mass balance reassessment of glaciers draining into the Abbot and Getz Ice Shelves of West Antarctica: Getz and Abbot Mass Balance Reassessment, Geophys. Res. Lett., 44, 7328–7337, https://doi.org/10.1002/2017GL073087, 2017.

Davis, C.: A Combined Surface/volume Scattering Retracking Algorithm for Ice Sheet Satellite Altimetry, in: Geoscience and Remote Sensing Symposium, 1992. IGARSS '92. International, vol. 2, pp. 969–971, https://doi.org/10.1109/IGARSS.1992.578311, 1992.

Davis, C.: A robust threshold retracking algorithm for measuring ice-sheet surface elevation change from satellite radar altimeters, Geoscience and Remote Sensing, IEEE Transactions on, 35, 974–979, https://doi.org/10.1109/36.602540, 1997.

Flament, T. and Rémy, F.: Dynamic thinning of Antarctic glaciers from along-track repeat radar altimetry, J. Glac., 58, 830–840, 2012.

Frappart, F., Legrésy, B., Niño, F., Blarel, F., Fuller, N., Fleury, S., Birol, F., and Calmant, S.: An ERS-2 altimetry reprocessing compatible with ENVISAT for long-term land and ice sheets studies, Remote Sens. Environ., 184, 558–581, https://doi.org/10.1016/j.rse.2016.07.037, 2016.

Fricker, H. and Padman, L.: Thirty years of elevation change on Antarctic Peninsula ice shelves from multimission satellite radar altimetry, J. Geophys. Res., 117, https://doi.org/10.1029/2011JC007126, 2012.

Gardner, A., Moholdt, G., Scambos, T., Fahnstock, M., Ligtenberg, S., van den Broeke, M., and Nilsson, J.: Increased West Antarctic and unchanged East Antarctic ice discharge over the last 7 years, The Cryosphere, 12, 521–547, https://doi.org/10.5194/tc-12-521-2018, 2018.

Groh, A. and Horwath, M.: The method of tailored sensitivity kernels for GRACE mass change estimates, Geophys. Res. Abstr., 18, EGU2016–12 065, 2016.

Groh, A., Ewert, H., Scheinert, M., Fritsche, M., Rülke, A., Richter, A., Rosenau, R., and Dietrich, R.: An Investigation of Glacial Isostatic Adjustment over the Amundsen Sea sector, West Antarctica, Global Planet. Change, 98–99, 45–53, https://doi.org/10.1016/j.gloplacha.2012.08.001, 2012.

Helm, V., Humbert, A., and Miller, H.: Elevation and elevation change of Greenland and Antarctica derived from CryoSat-2, The Cryosphere, 8, 1539–1559, https://doi.org/10.5194/tc-8-1539-2014, 2014.

Hogg, A., Shepherd, A., Cornford, S., Briggs, K., Gourmelen, N., Graham, J., Joughin, I., Mouginot, J., Nagler, T., Payne, A., Rignot, E., and Wuite, J.: Increased ice flow in Western Palmer Land linked to ocean melting, Geophys. Res. Lett., 44, 4159–4167, https://doi.org/10.1002/2016GL072110, 2017.

Horwath, M. and Dietrich, R.: Signal and error in mass change inferences from GRACE: the case of Antarctica, Geophys. J. Int., 177, 849–864, https://doi.org/10.1111/j.1365-246X.2009.04139.x, 2009.

Horwath, M., Legrésy, B., Rémy, F., Blarel, F., and Lemoine, J.-M.: Consistent patterns of Antarctic ice sheet interannual variations from ENVISAT radar altimetry and GRACE satellite gravimetry, Geophys. J. Int., 189, 863–876, https://doi.org/10.1111/j.1365-246X.2012.05401.x, 2012.

Hurkmans, R., Bamber, J., Sørensen, L., Joughin, I., Davis, C., and Krabill, W.: Spatiotemporal interpolation of elevation changes derived from satellite altimetry for Jakobshavn Isbræ, Greenland, J. Geophys. Res., 117, https://doi.org/10.1029/2011JF002072, 2012.

Ivins, E., James, T., Wahr, J., O. Schrama, E., Landerer, F., and Simon, K.: Antarctic contribution to sea level rise observed by GRACE with improved GIA correction, J. Geophys. Res. Solid Earth, 118, 3126–3141, https://doi.org/10.1002/jgrb.50208, 2013.

Joughin, I., Shean, D., Smith, B., and Dutrieux, P.: Grounding line variability and subglacial lake drainage on Pine Island Glacier, Antarctica, Geophys. Res. Lett., 43, 9093–9102, https://doi.org/10.1002/2016GL070259, 2016.

Kallenberg, B., Tregoning, P., Hoffmann, J., Hawkins, R., Purcell, A., and Allgeyer, S.: A new approach to estimate ice dynamic rates using satellite observations in East Antarctica, The Cryosphere, 11, 1235–1245, https://doi.org/10.5194/tc-11-1235-2017, 2017.

Khvorostovsky, K.: Merging and Analysis of Elevation Time Series Over Greenland Ice Sheet From Satellite Radar Altimetry, IEEE Trans. Geosci. Remote Sens., 50, 23–36, https://doi.org/10.1109/TGRS.2011.2160071, 2012.

Konrad, H., Gilbert, L., Cornford, S., Payne, A., Hogg, A., Muir, A., and Shepherd, A.: Uneven onset and pace of ice-dynamical imbalance in the Amundsen Sea Embayment, West Antarctica, Geophys. Res. Lett., https://doi.org/10.1002/2016GL070733, 2016.

Lacroix, P., Dechambre, M., Legrésy, B., Blarel, F., and Rémy, F.: On the use of the dual-frequency ENVISAT altimeter to determine snowpack properties of the Antarctic ice sheet, Remote Sens. Environ., 112, 1712–1729, https://doi.org/10.1016/j.rse.2007.08.022, 2008.

Legrésy, B. and Rémy, F.: Altimetric observations of surface characteristics of the Antarctic ice sheet, J. Glac., 43, 265–276, 1997.

Legrésy, B., Rémy, F., and Schaeffer, P.: Different ERS altimeter measurements between ascending and descending tracks caused by wind induced features over ice sheets, Geophys. Res. Lett., 26, 2231–2234, https://doi.org/10.1029/1999GL900531, 1999.

Legrésy, B., Papa, F., Rémy, F., Vinay, G., van den Bosch, M., and Zanife, O.-Z.: ENVISAT radar altimeter measurements over continental surfaces and ice caps using the ICE-2 retracking algorithm, Remote Sens. Environ., 85, 150–163, https://doi.org/10.1016/j.rse.2004.11.018, 2005.

Legrésy, B., Rémy, F., and Blarel, F.: Along track repeat altimetry for ice sheets and continental surface studies, in: Proc. Symposium on 15 years of Progress in Radar Altimetry, Venice, Italy, 13–18 March 2006, European Space Agency Publication Division, Noordwijk, The Netherlands, eSA-SP No. 614, paper No. 181, 2006.

Lenaerts, J., van Meijgaard, E., van den Broeke, M., Ligtenberg, S., Horwath, M., and Isaksson, E.: Recent snowfall anomalies in Dronning Maud Land, East Antarctica, in a historical and future climate perspective, Geophys. Res. Lett., 40, 2684–2688, https://doi.org/10.1002/grl.50559, 2013.

Li, X., Rignot, E., Morlighem, M., Mouginot, J., and Scheuchl, B.: Grounding line retreat of Totten Glacier, East Antarctica, 1996 to 2013, Geophys. Res. Lett., 42, 8049–8056, https://doi.org/10.1002/2015GL065701, 2015.

Li, X., Rignot, E., Mouginot, J., and Scheuchl, B.: Ice flow dynamics and mass loss of Totten Glacier, East Antarctica, from 1989 to 2015, Geophys. Res. Lett., 43, 6366–6373, https://doi.org/10.1002/2016GL069173, 2016.

Li, Y. and Davis, C.: Decadal Mass Balance of the Greenland and Antarctic Ice Sheets from High Resolution Elevation Change Analysis of ERS-2 and Envisat Radar Altimetry Measurements, in: IEEE International Geoscience & Remote Sensing Symposium, IGARSS 2008, July 8-11, 2008, Boston, Massachusetts, USA, Proceedings, pp. 339–342, IEEE, https://doi.org/10.1109/IGARSS.2008.4779727, 2008.

Ligtenberg, S., Helsen, M., and van den Broeke, M.: An improved semi-empirical model for the densification of Antarctic firn, The Cryosphere, 5, 809–819, https://doi.org/10.5194/tc-5-809-2011, 2011.

Martin, T., Zwally, H., Brenner, A., and Bindschadler, R.: Analysis and retracking of continental ice sheet radar altimeter waveforms, J. Geophys. Res., 88, 1608, https://doi.org/10.1029/JC088iC03p01608, 1983.

Martín-Español, A., Bamber, J., and Zammit-Mangion, A.: Constraining the mass balance of East Antarctica, Geophys. Res. Lett., 44, https://doi.org/10.1002/2017GL072937, 2017.

McMillan, M., Shepherd, A., Sundal, A., Briggs, K., Muir, A., Ridout, A., Hogg, A., and Wingham, D.: Increased ice losses from Antarctica detected by CryoSat-2, Geophys. Res. Lett., 41, 3899–3905, https://doi.org/10.1002/2014GL060111, 2014.

McMillan, M., Leeson, A., Shepherd, A., Briggs, K., Armitage, T., Hogg, A., Kuipers Munneke, P., van den Broeke, M., Noël, B., van de Berg, W., Ligtenberg, S., Horwath, M., Groh, A., Muir, A., and Gilbert, L.: A high-resolution record of Greenland mass balance, Geophys. Res. Lett., 43, 7002–7010, https://doi.org/10.1002/2016GL069666, 2016.

Mémin, A., Flament, T., Alizier, B., Watson, C., and Rémy, F.: Interannual variation of the Antarctic Ice Sheet from a combined analysis of satellite gravimetry and altimetry data, Earth Planet. Sci. Lett., 422, 150–156, https://doi.org/10.1016/j.epsl.2015.03.045, 2015.

Mouginot, J., Rignot, E., and Scheuchl, B.: Sustained increase in ice discharge from the Amundsen Sea Embayment, West Antarctica, from 1973 to 2013, Geophys. Res. Lett., 41, 1576–1584, https://doi.org/10.1002/2013GL059069, 2014.

Nilsson, J., Vallelonga, P., Simonsen, S., Sørensen, L., Forsberg, R., Dahl-Jensen, D., Hirabayashi, M., Goto-Azuma, K., Hvidberg, C., Kjaer, H., and Satow, K.: Greenland 2012 melt event effects on CryoSat-2 radar altimetry, Geophys. Res. Lett., 42, 3919–3926, https://doi.org/10.1002/2015GL063296, 2015.

Nilsson, J., Gardner, A., Sandberg Sørensen, L., and Forsberg, R.: Improved retrieval of land ice topography from CryoSat-2 data and its impact for volume-change estimation of the Greenland Ice Sheet, The Cryosphere, 10, 2953–2969, https://doi.org/10.5194/tc-10-2953-2016, 2016.

Paolo, F., Fricker, H., and Padman, L.: Constructing improved decadal records of Antarctic ice shelf height change from multiple satellite radar altimeters, Remote Sens. Environ., 177, 192–205, https://doi.org/10.1016/j.rse.2016.01.026, 2016.

Pritchard, H., Arthern, R., Vaughan, D., and Edwards, L.: Extensive dynamic thinning on the margins of the Greenland and Antarctic ice sheets, Nature, 461, 971–975, https://doi.org/10.1038/nature08471, 2009.

Rémy, F. and Parouty, S.: Antarctic Ice Sheet and Radar Altimetry: A Review, Remote Sensing, 1, 1212–1239, https://doi.org/10.3390/rs1041212, 2009.

Richter, A., Popov, S., Dietrich, R., Lukin, V., Fritsche, M., Lipenkov, V., Matveev, A., Wendt, J., Yuskevich, A., and Masolov, V.: Observational evidence on the stability of the hydro-glaciological regime of subglacial Lake Vostok, Geophys. Res. Lett., 35, L11 502, https://doi.org/10.1029/2008GL033397, 2008.

Richter, A., Popov, S., Fritsche, M., Lukin, V., Matveev, A., Ekaykin, A., Lipenkov, V., Fedorov, D., Eberlein, L., Schröder, L., Ewert, H., Horwath, M., and Dietrich, R.: Height changes over subglacial Lake Vostok, East Antarctica: Insights from GNSS observations, J. Geophys. Res. Earth Surf., 119, 2460–2480, https://doi.org/10.1002/2014JF003228, 2014.

Rignot, E.: Changes in ice dynamics and mass balance of the Antarctic ice sheet, Phil. Trans. R. Soc. Lond. A, 364, 1637–1655, 2006.

Rignot, E., Bamber, J., van den Broeke, M., Davis, C., Li, Y., van de Berg, W., and van Meijgaard, E.: Recent Antarctic ice mass loss from radar interferometry and regional climate modelling, Nature Geosci., 1, 106–110, https://doi.org/10.1038/ngeo102, 2008.

Rignot, E., Mouginot, J., and Scheuchl, B.: Ice Flow of the Antarctic Ice Sheet, Science, 333, 1427–1430, https://doi.org/10.1126/science.1208336, 2011.

Rignot, E., Mouginot, J., Morlighem, M., Seroussi, H., and Scheuchl, B.: Widespread, rapid grounding line retreat of Pine Island, Thwaites, Smith, and Kohler glaciers, West Antarctica, from 1992 to 2011, Geophys. Res. Lett., 41, 3502–3509, https://doi.org/10.1002/2014GL060140, 2014.

Roemer, S., Legrésy, B., Horwath, M., and Dietrich, R.: Refined analysis of radar altimetry data applied to the region of the subglacial Lake Vostok / Antarctica, Remote Sens. Environ., 106, 269–284, https://doi.org/10.1016/j.rse.2006.02.026, 2007.

Schröder, L., Richter, A., Fedorov, D., Eberlein, L., Brovkov, E., Popov, S., Knöfel, C., Horwath, M., Dietrich, R., Matveev, A., Scheinert, M., and Lukin, V.: Validation of satellite altimetry by kinematic GNSS in central East Antarctica, The Cryosphere, 11, 1111–1130, https://doi.org/10.5194/tc-11-1111-2017, 2017.

Scott, R., Baker, S., Birkett, C., Cudlip, W., Laxon, S., Mantripp, D., Mansley, J., Morley, J., Rapley, C., Ridley, J., Strawbridge, F., and Wingham, D.: A comparison of the performance of the ice and ocean tracking modes of the ERS-1 radar altimeter over non-ocean surfaces, Geophys. Res. Lett., 21, 553–556, https://doi.org/10.1029/94GL00178, 1994.

Shepherd, A., Ivins, E., A, G., Barletta, V., Bentley, M., Bettadpur, S., Briggs, K., Bromwich, D., Forsberg, R., Galin, N., Horwath, M., Jacobs, S., Joughin, I., King, M., Lenaerts, J., Li, J., Ligtenberg, S., Luckman, A., Luthcke, S., McMillan, M., Meister, R., Milne, G., Mouginot, J., Muir, A., Nicolas, J., Paden, J., Payne, A., Pritchard, H., Rignot, E., Rott, H., Sorensen, L., Scambos, T., Scheuchl, B., Schrama, E., Smith, B., Sundal, A., van Angelen, J., van de Berg, W., van den Broeke, M., Vaughan, D., Velicogna, I., Wahr, J., Whitehouse, P., Wingham, D., Yi, D., Young, D., and Zwally, H.: A Reconciled Estimate of Ice-Sheet Mass Balance, Science, 338, 1183–1189, https://doi.org/10.1126/science.1228102, 2012.

Shepherd, A., Ivins, E., Rignot, E., Smith, B., van den Broeke, M., Velicogna, I., Whitehouse, P., Briggs, K., Joughin, I., Krinner, G., Nowicki, S., Payne, T., Scambos, T., Schlegel, N., A, G., Agosta, C., Ahlstrøm, A., Babonis, G., Barletta, V., Blazquez, A., Bonin, J., Csatho, B., Cullather, R., Felikson, D., Fettweis, X., Forsberg, R., Gallee, H., Gardner, A., Gilbert, L., Groh, A., Gunter, B., Hanna, E., Harig, C., Helm, V., Horvath, A., Horwath, M., Khan, S., Kjeldsen, K., Konrad, H., Langen, P., Lecavalier, B., Loomis, B., Luthcke, S., McMillan, M., Melini, D., Mernild, S., Mohajerani, Y., Moore, P., Mouginot, J., Moyano, G., Muir, A., Nagler, T., Nield, G., Nilsson, J., Noel, B., Otosaka, I., Pattle, M., Peltier, W., Pie, N., Rietbroek, R., Rott, H., Sandberg-Sørensen, L., Sasgen, I., Save, H., Scheuchl, B., Schrama, E., Schröder, L., Seo, K.-W., Simonsen, S., Slater, T., Spada, G., Sutterley, T., Talpe, M., Tarasov, L., van de Berg, W., van der Wal, W., van Wessem, M., Vishwakarma, B., Wiese, D., and Wouters, B.: Mass balance of the Antarctic Ice Sheet from 1992 to 2017, Nature, 558, 219–222, https://doi.org/10.1038/s41586-018-0179-y, 2018.

Studinger, M.: IceBridge ATM L4 Surface Elevation Rate of Change, Version 1. Updated 2017., Boulder, Colorado USA. NASA National Snow and Ice Data Center Distributed Active Archive Center, https://doi.org/10.5067/BCW6CI3TXOCY, [date accessed: 2018-02-28], 2014.

Thomas, E., Hosking, J., Tuckwell, R., Warren, R., and Ludlow, E.: Twentieth century increase in snowfall in coastal West Antarctica, Geophys. Res. Lett., 42, 9387–9393, https://doi.org/10.1002/2015GL065750, 2015.

Thomas, R., Davis, C., Frederick, E., Krabill, W., Li, Y., Manizade, S., and Martin, C.: A comparison of Greenland ice-sheet volume changes derived from altimetry measurements, J. Glac., 54, 203–212, https://doi.org/10.3189/002214308784886225, 2008.

van Wessem, J., van de Berg, W., Noël, B., van Meijgaard, E., Amory, C., Birnbaum, G., Jakobs, C., Krüger, K., Lenaerts, J., Lhermitte, S., Ligtenberg, S., Medley, B., Reijmer, C., van Tricht, K., Trusel, L., van Ulft, L., Wouters, B., Wuite, J., and van den Broeke, M.: Modelling the climate and surface mass balance of polar ice sheets using RACMO2 – Part 2: Antarctica (1979–2016), The Cryosphere, 12, 1479–1498, https://doi.org/10.5194/tc-12-1479-2018, 2018.

Wingham, D., Rapley, C., and Griffiths, H.: New techniques in satellite altimeter tracking systems, in: ESA Proceedings of the 1986 International Geoscience and Remote Sensing Symposium(IGARSS'86) on Remote Sensing: Today's Solutions for Tomorrow's Information Needs,, vol. 3, pp. 1339–1344, 1986.

Wingham, D., Ridout, A., Scharroo, R., Arthern, R., and Shum, C.: Antarctic Elevation Change from 1992 to 1996, Science, 282, 456–458, https://doi.org/10.1126/science.282.5388.456, 1998.

Wingham, D., Francis, C., Baker, S., Bouzinac, C., Brockley, D., Cullen, R., Chateau-Thierry, P. d., Laxon, S., Mallow, U., Mavrocordatos, C., Phalippou, L., Ratier, G., Rey, L., Rostan, F., Viau, P., and Wallis, D.: CryoSat: A mission to determine the fluctuations in Earth's land and marine ice fields, Adv. Space Res., 37, 841–871, https://doi.org/10.1016/j.asr.2005.07.027, 2006a.

Wingham, D., Shepherd, A., Muir, A., and Marshall, G.: Mass balance of the Antarctic ice sheet, Phil. Trans. R. Soc. Lond. A, 364, 1627–1635, https://doi.org/10.1098/rsta.2006.1792, 2006b.

Wouters, B., Bamber, J., van den Broeke, M., Lenaerts, J., and Sasgen, I.: Limits in detecting acceleration of ice sheet mass loss due to climate variability, Nature Geosci., 6, 613–616, https://doi.org/10.1038/ngeo1874, 2013.

Wouters, B., Martín-Español, A., Helm, V., Flament, T., van Wessem, J., Ligtenberg, S., van den Broeke, M., and Bamber, J.: Dynamic thinning of glaciers on the Southern Antarctic Peninsula, Science, 348, 899–903, https://doi.org/10.1126/science.aaa5727, 2015.

Zwally, H., Giovinetto, M., Li, J., Cornejo, H., Beckley, M., Brenner, A., Saba, J., and Yi, D.: Mass changes of the Greenland and Antarctic ice sheets and shelves and contributions to sea-level rise: 1992-2002, J. Glac., 51, 509–527, https://doi.org/10.3189/172756505781829007, 2005.

Zwally, H., Li, J., Robbins, J., Saba, J., Yi, D., and Brenner, A.: Mass gains of the Antarctic ice sheet exceed losses, J. Glac., 61, 1019–1936, 2015.